Dissociation in 2D Material Photovoltaic Devices: The Role of Intralayer and Interlayer Excitons

MSc Thesis

Gabriella Mentasti Meza

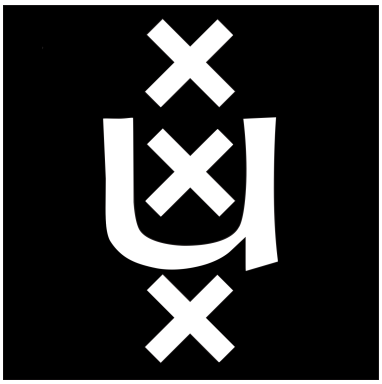

Institute of Physics
University of Amsterdam
July 2025

Daily Supervisors: Tom Hoekstra MSc, Bernardo S. Dias MSc
Supervisor: Dr. Jorik van de Groep
Examiner: Prof. dr. Peter Schall

Abstract

Research into photovoltaic technologies continues to be driven by the desire to transition towards renewable energy production. Recently, thin-film photovoltaics, notably those made with two-dimensional materials, have garnered attention due to their mechanical flexibility and lightweight nature. Transition metal dichalcogenides, in particular, are attractive candidates due to their high absorption coefficients, strong light-matter interactions, and excitonic properties. However, current fabrication techniques remain limited by the quality or the size of the monolayer produced. Therefore, this thesis investigates the fabrication and characterisation of a large-area WS_2/WSe_2 photovoltaic device. We utilise gold-assisted exfoliation to obtain large-area monolayers before exploring the new transfer method, which employs low-density polyethylene and oleic acid to achieve high optical quality. We find that the new transfer method not only produces large-area samples but also yields monolayers with narrow photoluminescence excitonic linewidths (~27 meV). Raman spectroscopy confirms the successful stamping of the WS_2/WSe_2 heterostructure. The heterostructure displays interlayer excitonic coupling on top of the regular intralayer excitons, as indicated by the two distinct peaks at ~840 and ~910 nm. A power-law exponent of 0.78 corroborates this result. The reflectivity spectrum provides further insight into interlayer exciton formation, with results suggesting a two-step excitation mechanism. The heterostructure is then integrated onto gold contacts and electrically characterised. The current-voltage measurement under illumination demonstrates a high resistance (on the order of GΩ), resulting in a linear behaviour. Nevertheless, when measuring the external quantum yield, we observe enhanced absorption at WS_2 excitonic wavelengths. Hence, although a photovoltaic device could not be realised, this thesis explores a reproducible method to fabricate large-area 2D devices that exhibit strong excitonic behaviours. The results serve as a basis for further optimising two-dimensional optoelectronic devices, particularly those composed of WS_2 and WSe_2.

Contents

Chapter 1

Introduction

Achieving carbon neutrality by 2050, as outlined in the Paris Agreement (COP21), requires a significant transition from fossil fuels, such as oil, natural gas, and coal, to renewable energy sources [1]. Among the renewable energy technologies, photovoltaics (PV) present a distinct advantage due to their affordability, modularity, and ease of implementation at an individual level [2]. This is particularly important when considering energy consumption across different sectors: while industry remains the largest consumer, transport and buildings are the second and third largest, respectively [3]. Achieving the renewable energy transition in these two sectors could prove imperative for carbon neutrality, and the integration of PV technologies onto buildings, vehicles, and textiles could facilitate it.

However, the rigidity and weight of current commercial PV limit their applicability on curved and non-load-bearing structures. Thin-film PV technologies have gained attention due to their mechanical flexibility and limited thickness, which allows integration into a myriad of objects and situations. Notably, the integration of thin-film PV onto buildings has been highlighted by consortia such as SolarNL as a critical step in the broader adoption of PV technology [4]. Yet, to accomplish this large-scale application demands continued research into novel materials.

Two-dimensional (2D) materials are one of those novel emergent resources, spurred by the successful isolation of graphene by Geim and Novoselov in 2004 [5]. In particular, transition metal dichalcogenides (TMDCs) exhibit valuable properties for optoelectronic applications. Their strong light-matter interaction and high absorption coefficients make them excellent thin absorber layers [6], an attractive feature in the advancement of PV. Furthermore, TMDCs are able to form van der Waals heterostructures (HS). The customisability of these HS, based on material choice, allows for greater tunability of the optical and electrical properties [6], such as fabricating HS with band gaps that approach the optimal value for solar energy conversion [6]. Moreover, these staggered gap heterostructures facilitate efficient charge separation, thereby enhancing photovoltaic efficiency [7].

Despite these promising characteristics, the development of 2D material devices remains limited by the 2D material fabrication methods. Bottom-up methods, such as chemical vapour deposition (CVD), offer scalability but are likely to produce lower-quality materials due to issues like inhomogeneous growth [8]. Conversely, mechanical exfoliation produces monolayers with high-quality excitonic responses but is limited by their size, typically tens of microns [9]. Hence, investigating a method which bridges the gap is crucial for device prototyping and, eventually, its commercialisation.

In this thesis, we fabricate a high-quality large-area 2D heterostructure device by combining gold-assisted exfoliation (GAE) and a novel low-density polyethylene (LDPE)-based transfer method. We investigate the optical and electrical behaviour of intralayer and interlayer excitons (IX) in the resultant tungsten disulphide (WS_2) and tungsten diselenide (WSe_2) HS. Specifically, we aim to understand how the excitonic properties present in a large-area 2D HS photovoltaic device influence its light absorption, charge generation, and charge collection.

The structure of this thesis is as follows. In Chapter 2, we introduce 2D materials and excitons, followed by a brief explanation of photodetection and a brief overview of current research on TMDC-based PV. We conclude by examining the junction created by TMDC pairings, from which we select WS_2 and WSe_2 as the ideal materials. Chapter 3 outlines the optical and electrical characterisation techniques used to probe the excitonic dynamics and the light-induced response in a device. Next, in Chapter 4, we describe the exfoliation and transfer processes used to obtain high-quality, large-area monolayers reliably. Thereafter, in Chapter 5, we fabricate and optically characterise a WS_2/WSe_2 heterostructure. Following this, Chapter 6 details the design, fabrication, and optically and electronically characterisation of a device composed of a WS_2/WSe_2/hBN heterostructure integrated onto gold contacts. Finally, in Chapter 7, we summarise the main findings and propose future research directions.

Chapter 2

2D Semiconductors

In this chapter, we begin by introducing 2D semiconductors with a particular emphasis on transition metal dichalcogenides (TMDCs) (2.1). Then we discuss excitons in TMDCs and their effect (2.2). After, we explore the use of transition metal dichalcogenides for photogeneration, the current designs, and the limits of prevalent monolayer fabrication methods for photovoltaics (2.3). Finally, we highlight why WS_2 and WSe_2 were selected for our PV structure (2.4).

2.1 2D Semiconductors

2D materials are materials composed of covalently-bonded atomic layers held together by weak van der Waals forces [10]. This weak interlayer interaction enables the reduction of a 2D crystal to a single atomic layer, referred to as a monolayer. This process was first published in 2004 by Geim and Novoselov, who exfoliated graphite down to a graphene monolayer using Scotch-Tape [5]. From there, the field of possibilities for 2D material monolayers has expanded, with more than 10,000 different 2D compounds found computationally [11], ranging from conductors like graphite to insulators like hexagonal boron nitride (hBN) and, more importantly for this project, semiconductors like TMDCs.

These TMDCs are composed of a transition metal, M, and two group VI elements, X, with a chemical formula of MX_2. In a monolayer limit, these materials range from 6-7 Å (0.6-0.7 nm) in width composed of a layer of hexagonally arranged transition metal atoms sandwiched between two layers of chalcogenide atoms [10]. As such, the geometric arrangement of TMDCs, although octahedral in some cases, is usually trigonal prismatic as shown in Fig. 2.1a).

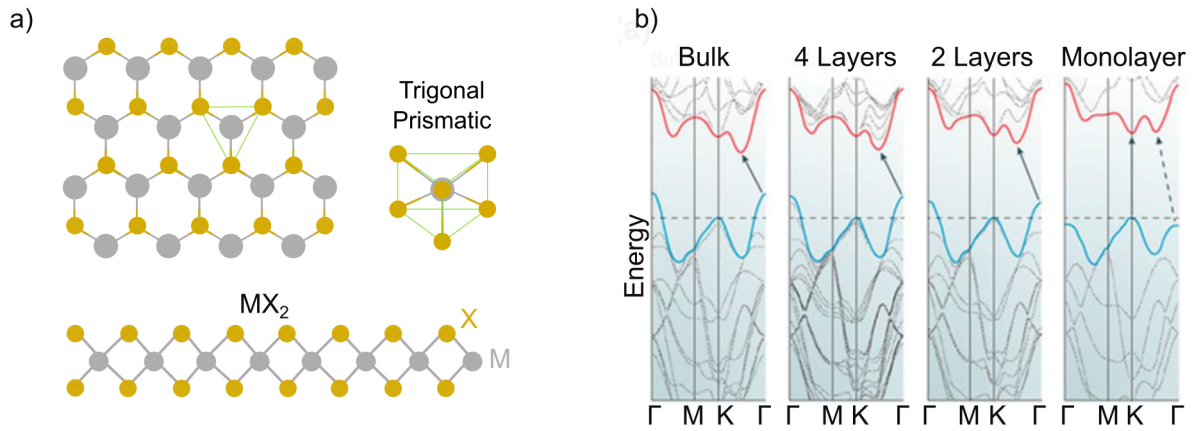

Figure 2.1: (a) Structure of a trigonal prismatic TMDC. Inspired by [12, 13]. (b) Density functional theory-calculated band structures going from bulk to monolayer. The arrows connecting the valence band maxima to the conduction band minima indicate the fundamental band gaps for each configuration. The figure is adapted from [14].

Nearing the monolayer limit, TMDCs exhibit an intriguing change in properties as a consequence of a changing

bandgap. The gradual change from bulk to monolayer is demonstrated in Fig. 2.1b). The bandgap diagrams, calculated using density functional theory, illustrate the gradual shift from a diagonal (indirect and phonon-mediated) transition to a vertical (direct) transition when going from bulk to monolayer. This transformation is suggested to be caused by the decreased shielding and increased quantum confinement resulting from the thinning of a TMDC, which causes the indirect band gap to widen [10]. Comparatively, the direct band gap remains the same, and becomes the more energetically favourable transition. Optically, this transition from phonon-mediated excitation to non-photon-mediated excitation enhances light absorption and emission efficiency.

Beyond changing to a direct optical transition, the reduction in thickness also leads to the formation of strongly bound excitons that are stable even at room temperature. This stability, enhanced by reduced dielectric screening and enhanced confinement experienced by 2D materials, makes monolayer TMDCs intriguing materials to explore in terms of excitons, optics, and optoelectronics.

2.2 Excitons

Excitons are electron-hole pairs bounded together by Coulombic forces, where the electron is excited into the conduction band while the hole remains in the valence band [15]. In a monolayer, the formation of excitons lowers the fundamental bandgap, such that:

$$E_{opt} = E_g - E_b, \tag{2.1}$$

where E_g is the bandgap energy and E_b is the exciton binding energy. Evidently, the formation energy of these intralayer excitons is lower than for unbound electron-hole pairs, and is therefore favoured in TMDC monolayers.

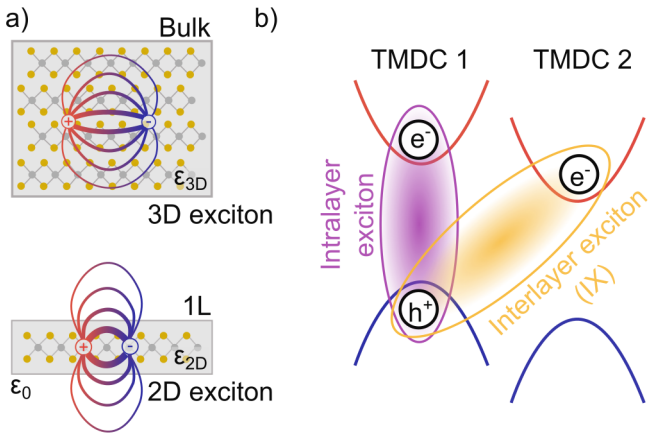

Figure 2.2: a) Real-space representation of excitons (bound electron-hole pairs) in bulk and monolayer (1L) TMDCs. The vacuum permittivity is indicated by ε_0, while ε_{3D} and ε_{2D} indicate the respective dielectric constants. The figure is inspired by [16]. b) Illustration of intralayer and interlayer (IX) excitons.

The strength of the electron-hole (Fig. 2.2a) coupling of intralayer excitons is attributable to the mass, dielectric screening, and electron-hole separation in the material [10]. In more restricted dimensions, the material experiences reduced dielectric screening, yielding less effective shielding of the electric field produced by the electron-hole pair. Furthermore, the reduction from three dimensions to two dimensions causes the electron-hole pair to be physically closer together, resulting in a further increase in their binding energy. Therefore, while excitons exist in both bulk and monolayer, intralayer excitons are less distinct at room temperature for bulk TMDCs. This is due to additional optical transitions and carrier relaxation channels, which cause the resonance features to broaden [17]. Moreover, due to the lower exciton binding energy of 50 meV in bulk [16] compared to the monolayer (on the order of 500 meV [10]), the

thermal energy at room temperature of $k_B T = 25$ meV is sufficient to dissociate the excitons in bulk, making them more unstable. Consequently, as monolayer TMDCs possess highly stable excitons, they are ideal for investigating exciton dynamics and other optical properties.

Another property of TMDCs is their lack of dangling bonds, which, along with their layered nature, allows for monolayers to be readily stacked in so-called Van der Waals heterostructures. In these heterostructures, a new type of exciton can be formed, the interlayer exciton (IX), with the electron in one material and the hole in the other, as shown in Fig. 2.2b). In this scenario, the optical band gap is defined as:

$$E_{g,\mathrm{IX}} = E_{c,\mathrm{min}} - E_{v,\mathrm{max}}, \tag{2.2}$$

where $E_{c,\mathrm{min}}$ is the lowest conduction band and $E_{v,\mathrm{max}}$ is the highest valence band, regardless of material.

In contrast to intralayer excitons, interlayer excitons have a lower binding energy (~200 meV [18]) due to the larger spatial separation of the electron–hole pair. They are therefore less stable at room temperature. Hence, their spectral response at room temperature is often diminished, causing considerable research to focus on the detailed examination of interlayer excitons in low-temperature regimes [19, 20, 21, 22]. The existence of an additional absorption pathway, in the form of producing interlayer excitons at room temperature, makes TMDCs attractive materials for a variety of optoelectronic devices. Notably, the need for two monolayers to create a homobilayer or heterobilayer adds an aspect of customizability depending on the intended use.

2.3 2D Solar Cells

2.3.1 Photogeneration

In semiconductors, a photon with energy, E_{ph}, larger than the band gap, E_g, may be absorbed by an electron that is excited from the occupied valence band to an empty state in the conduction band [7]. The energy ΔE for a photon to successfully produce this transition is:

$$\Delta E = \frac{h \cdot c}{\lambda}, \tag{2.3}$$

where h is Planck's constant, c is the speed of light, and λ is the photon wavelength. The minimum energy required is $\Delta E = E_g$, which results in the excitation of an electron in an electron-hole pair to the conduction band. The electron eventually relaxes back to the valence band and, upon recombination with a hole, emits a photon with energy E_g.

The ability to limit the charge recombination and the ensuing emission is vital for PV. Hence, traditional solar cells are typically composed of p-n junctions, where p and n refer to the dominant carriers of electric charge in the material, either holes (p) or electrons (n). This also indicates where the Fermi energy level E_F of each material resides within its band structure, with n-type materials having E_F close to the conduction band due to having more electrons, while p-type materials have their E_F closer to the valence band as a result of an increased number of holes [7]. Due to a mismatch in E_F, when the interface is created, the bands shift so that the Fermi energy levels of both materials coincide. To keep a material's work function and electron affinity the same, the result is a shift of the band structures as a whole, such that the bands at the interface bend. This bending is caused by the redistribution of charges from high to low concentrations [7], and induces a depletion region.

The expected shift, and more importantly, the final alignment of the conduction and valence bands at the interface are crucial considerations. Typically, the band alignment comes in the form of one of three configurations: Fig. 2.3a) type I - straddle gap, 2.3b) type II - staggered gap, and 2.3c) type III - broken gap [7]. However, for heterojunction PVs, the objective is to obtain a staggered gap heterojunction where the lower-energy conduction band, E_c, and higher-energy valence band, E_v, are in opposite materials. By offsetting the bands, electrons migrate into the lower-energy conduction band while holes move into the higher-energy valence band, which enhances charge separation and

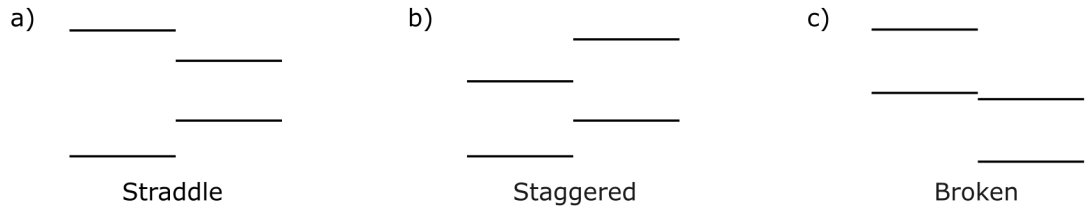

Figure 2.3: Illustrations of the different gap configurations possible in a heterostructure. a) Straddle gap. b) Staggered gap. c) Broken gap.

suppresses recombination. With the electrons and holes separated, if connected to metal contacts, the electrons can diffuse through the material towards the contacts, creating an electron flow that results in current.

It is not necessary to have one p-type and one n-type material to create an effective staggered gap heterojunction PV. A heterojunction is comprised of two materials with different band gaps, E_g, whether due to the material's intrinsic characteristic or doping [7]. Hence, although most TMDCs are typically intrinsically n-doped [23], a heterojunction of two different TMDCs (with different E_g) is still a valid choice in terms of their band gaps. Furthermore, their ability to stack on top of each other through van der Waals forces does not result in typical band bending. This is due to the absence of dangling bonds leading to fewer interface states and Fermi-level pinning [24]. Thus, to create a staggered gap heterojunction, one only needs to compare the band structures of the constituent materials, with each combination yielding different interlayer exciton energies.

2.3.2 Prior 2D Photovoltaic Designs

Photovoltaics convert optical energy to electrical energy, making a material's absorption and bandgap critical properties to consider. Figure 2.4a) presents a plot of different materials according to their absorption coefficient, the absorption per cm thickness at 600 nm, against the band gap. Compared to current commercial PV materials like Silicon (Si) with an absorption coefficient of $4{\cdot}10^3$ cm^{-1}, both bulk and monolayer TMDCs demonstrate a higher absorption with a coefficient ranging from $1{\cdot}10^5$ to $4{\cdot}10^5$ cm^{-1}. This is an increase by a factor of 100, meaning that TMDCs require small thicknesses to surpass the expected absorption length. Additionally, the bandgap of the monolayers aligns closely with the optimum band gap for maximum (broad) solar (wavelength range) absorption according to the Shockley-Queisser theoretical limit of E_g = 1.34 eV [6]. Hence, due to their high absorption coefficient, low weight, high flexibility, and near-optimal band gap energy, TMDCs are significant materials to investigate in PV, particularly for the development of light and flexible films.

Currently, the devices with the highest power conversion efficiencies are those composed of nanometer-thick layers, which can efficiently convert between ~1-5% [25] of the power or the use of TMDCs as absorptive layers on top of other semiconductor materials like silicon [26] to produce tandem cells. However, a lot of research focuses on using single TMDC monolayers in various configurations to create a metal-semiconductor (Schottky) junction PV. One such case is photovoltaics made of molybdenum disulfide (MoS_2) and asymmetric metal contacts of pairings like Pt-Ti [9] (Fig. 2.4b), and Pd-Au [27], and Pd-Cr/Au [28]. The asymmetric contacts, defined here as electrodes made of different metals with different work functions, are used to ensure charge separation in single-material photovoltaic devices, while also influencing the power conversion efficiency experienced. Currently, these single-monolayer devices have shown to produce power conversion efficiencies of a maximum of 0.46% [29].

In other cases, higher power conversion efficiencies are achieved by exploiting the ability of 2D materials to stack onto one another, creating heterostructures that support both intralayer and interlayer excitons. This is a crucial consideration in photocurrent generation, as efficiency is dependent on lattice matching. Materials in typical PV heterostructures are carefully selected so that their lattice constants match. This is due to lattice mismatch, resulting in dislocations and disfigurations of the material structure at the interface, and hence, producing defects such as traps [7], which decrease efficiency. In contrast, any combination of 2D material, such as the WSe_2/MoS_2 [8] shown in Fig.

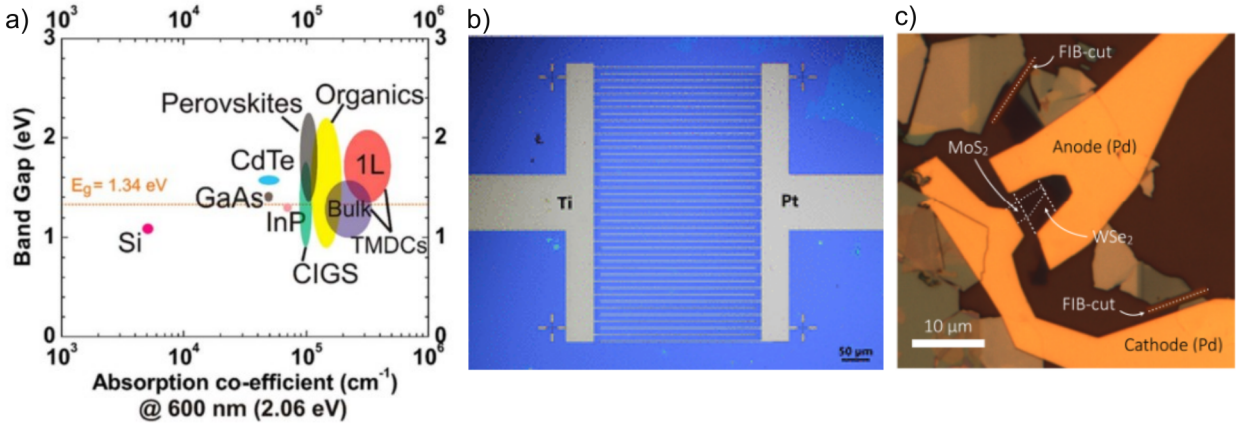

Figure 2.4: a) Plot showing potential semiconductor materials for photovoltaic use with respect to their absorption coefficient and their band gap. TMDCs are shown both in bulk and monolayer (1L). The orange dotted line E_g indicates the Shockley-Queisser band gap for maximum theoretical efficiency. Taken from [6]. b) CVD-grown MoS_2 monolayer photovoltaic on top of titanium and platinum contacts. Taken from [9]. c) Mechanically exfoliated MoS_2/WSe_2 heterostructure photovoltaic fabricated on palladium contacts. Taken from [8].

2.4, can become a viable configuration for PV.

2.4 Material Selection for 2D Heterostructure Photovoltaic Device

The ability to change the interlayer band gap by selecting the materials offers a plethora of heterostructure possibilities. Yet, given the focus on photovoltaics, it is necessary to evaluate the band gap in terms of its charge separation efficiency, and ultimately the achievable open-circuit voltage (V_{OC}). In PV devices, the open-current voltage is the maximum voltage the device produces when no current is drawn, and typically reflects the difference in quasi-Fermi levels for electrons and holes under illumination—setting an upper limit related to, but always less than, the material's band gap. However, the ideal maximum power (P_{ideal}) is defined as:

$$P_{ideal} = I_{SC} \cdot V_{OC}, \tag{2.4}$$

where I_{SC} is the short-circuit current, the rate of flow of electrons moving through a circuit without an opposing voltage. Hence, the ideal maximum power of any device is dictated by a compromise between the open-circuit voltage and the short-circuit current. This trade-off is illustrated in Fig. 2.4a) where the ideal theoretical band gap of 1.34 eV from the Shockley-Queisser limit arises from balancing the effect of the bandgap on the open-circuit voltage and short-circuit current: the larger the bandgap, the greater the open-circuit voltage at the cost of reducing the fraction of sunlight that can be absorbed (because fewer photons have enough energy to excite electrons across the band gap), which in turn lowers the short-circuit, and vise versa [7].

Figure 2.5 presents a comparison of the conduction and valence bands for a selection of the most common TMDC heterostructures [31, 30]. This analysis is conducted to ensure that all conduction and valence band offsets are greater than the thermal energy at room temperature (~25 meV [15]). A band offset smaller than this could lead to ineffective charge separation as thermally excited electrons have sufficient energy to overcome the potential barrier and move across the junction unimpeded. As such, the $MoSe_2/WS_2$ heterostructure is eliminated from the candidate pool due to a conduction band offset of 10 meV.

From there, the selection is made by considering the band gap energy closest to the theoretical optimum of 1.36 eV. The outcome is two distinct frontrunners: $MoSe_2/WSe_2$ and WS_2/WSe_2 with an $E_{g,IX}$ of 1.29 and 1.28 eV, shown

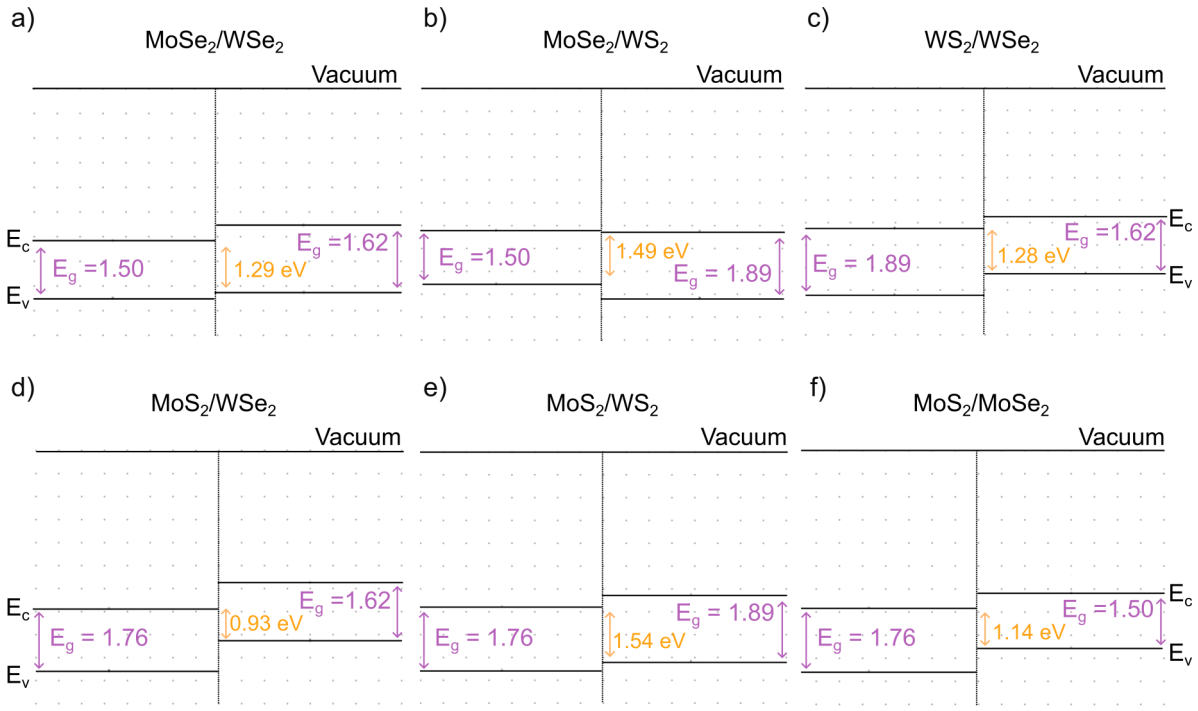

Figure 2.5: Illustrations showing the different TMDC pairings to form heterostructures when using WS_2, WSe_2, MoS_2, and $MoSe_2$. The purple values indicate each material's fundamental band gap (taken from [30]) while the yellow values indicate the calculated interlayer band gaps.

respectively in Fig. 2.5a) and 2.5e). While the WS_2/WSe_2 heterostructure has already been explored in photovoltaic applications [32], we selected it not only due to its potential photovoltaic performance, but also because of its suitability to study both intralayer and interlayer excitons. Among the other TMDCs, WS_2 has the A-exciton resonance with the strongest oscillator strength and a clear spectral separation from its B-exciton [17], which facilitates the monitoring of individual spectral shifts and excitonic intensity changes during our measurements. Accordingly, in the following chapter we detail the optical characterisation methods (Raman spectroscopy, photoluminescence spectroscopy, and reflectivity) we employ to examine our 2D heterostructure and its optical response.

Chapter 3

Optical and Electrical Characterization Methodology

In this chapter, we describe the optical and electrical characterisation methods used to examine our TMDC monolayers and subsequent heterostructures, what they are used for, and the setups. First, we discuss what Raman spectroscopy entails, how it is measured, and what the ensuing results mean for a sample (3.1). Next, we explain three different types of photoluminescence (dark-field, wide-field, and temperature-dependent) and their corresponding setups (3.2). We later detail what reflectivity measurements entail and how they are conducted throughout this project (3.3). Finally, we delve into the principles and setup of current-voltage (IV) and external quantum yield (EQE) measurements, used for electrical characterisation

3.1 Raman Spectroscopy

Raman spectroscopy consists of using light to excite the vibration modes in materials, where the atoms and the structure of the material generate unique modes that enable the identification of materials and effects such as strain and doping. Each peak can be categorised into modes such as E_{2g}, A_{1g}, and B_{2g}, illustrated in Fig. 3.1a), where each has a corresponding in-plane or out-of-plane movement [33]. The notation of each mode comes from group theory [34]. Figure 3.1b) shows an example of Raman spectroscopy of bilayer and monolayer WSe_2, with the three aforementioned modes displayed.

E_{2g} is indicative of a Raman-active in-plane vibration of our molecule [35]. Modes can be Raman-active, IR-active, or even inactive. This is a consequence of whether the allowed vibrations match the molecule's symmetry. Apart from that, the in-plane direction of the mode also means that this particular mode has low sensitivity to the thickness of our TMDC due to its direction of vibration [35]. Furthermore, examining the point group theory in more detail, the "2" indicates that the vibration is antisymmetric with respect to a specific mirror plane. In this case, the mirror plane lies parallel to the TMDC surface. The opposite, the symmetric relation is indicated by a "1". Lastly, "E" indicates that the mode is doubly degenerate, two vibrations in opposite directions [34]. Hence, E_{2g} represents a vibrational mode that is doubly degenerate, antisymmetric, and in-plane.

On the other hand, both A_{1g} and B_{2g} refer to the out-of-plane vibrations of molecules [35], which means that they are susceptible to changes in thickness, such that each subsequent monolayer provokes a distinct shift in intensity. Another similarity between modes is that the labels "A" and "B" indicate they are non-degenerate modes, but differentiate themselves from each other due to their symmetric and antisymmetric rotational symmetries along the principal axis. Accordingly, mode B_{2g} also indicates an antisymmetric vibration with respect to the plane, as noted by the "2" shared with the E_{2g} mode. Moreover, the most significant difference between B_{2g} and the other modes is illustrated in Fig. 3.1b): B_{2g} is Raman-inactive in the monolayer limit since this mode, which corresponds to interlayer breathing, requires an inversion symmetry which only occurs with multiple layers for TMDCs [34]. Hence, the Raman modes detected can tell us about the vibrations of the molecules, whether it is a monolayer, and the physical effect of stacking monolayers on top of each other.

For this project, Fig. 3.2 depicts the setup we use to measure the Raman spectrum. We use a WiTec α300K confocal microscope in dark-field mode with a 100 times Zeiss EC Epiplan–Neofluan (NA = 0.9) microscope objective. The

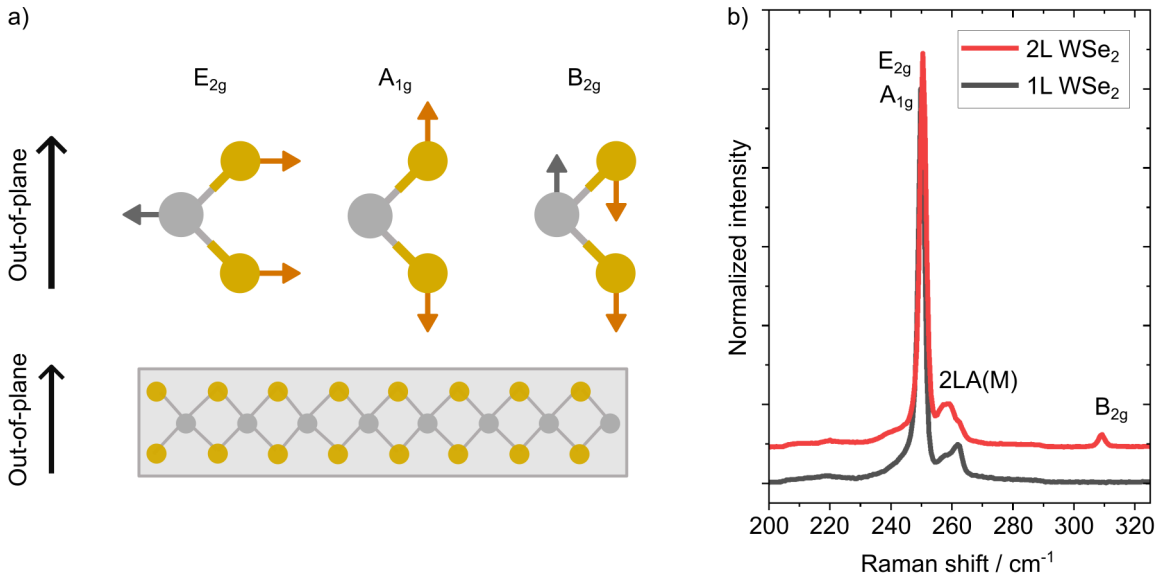

Figure 3.1: a) Representation of the vibrational modes visible in TMDCs in relation to the monolayer plane. The arrows indicate the direction of vibrations for each atom. b) Raman spectroscopy of a WSe_2 bilayer and monolayer, with the Raman modes indicated in the plot. a) is inspired by and b) is adapted from [33]

excitation source is a 532 nm fibre-coupled diode laser. After its incidence on the sample, we use a 532 nm long-pass filter to remove any reflected laser light so that, after being chromatically dispersed by a WiTec UHUTS300 SMFC VIS Spectrograph (1800 grooves/mm), only the TMDC response is measured on an Andor Newton EMCCD camera cooled to -60 °C.

3.2 Photoluminescence Spectroscopy

3.2.1 Room-Temperature Photoluminescence Spectroscopy

Photoluminescence (PL) spectroscopy is an optical technique that probes the electronic response of a material by measuring the photon emission after laser excitation. This optical response is a result of an excitation-recombination-emission cycle. The excitation by incident laser photons with energies equal to or greater than the optical band gap, E_{opt}, of the material, promotes electrons from the valence band into higher energy states. These electrons will eventually recombine with the holes in the valence band, emitting photons with lower energy than the incident photon due to non-radiative losses. In TMDCs, as the electron relaxes back to the valence band, it emits a photon with the same energy as the exciton binding energy. A spectrometer then detects these emissions. Hence, apart from using 600 grooves/mm, photoluminescence spectroscopy at room temperature employs the same setup as described for Raman spectroscopy, depicted in green in Fig. 3.2.

3.2.2 Wide-Field Photoluminescence Spectroscopy

Wide-field photoluminescence spectroscopy is conducted using a laser whose incidence is spatially expanded to illuminate the sample uniformly. Unlike focused PL, which uses a concentrated beam, wide-field PL spectroscopy maintains a fixed angle of incidence across the whole region, causing the power to be distributed over a broader area. However, thanks to the strong exciton luminescence displayed by 2D materials, the reduced power can still induce strong pho-

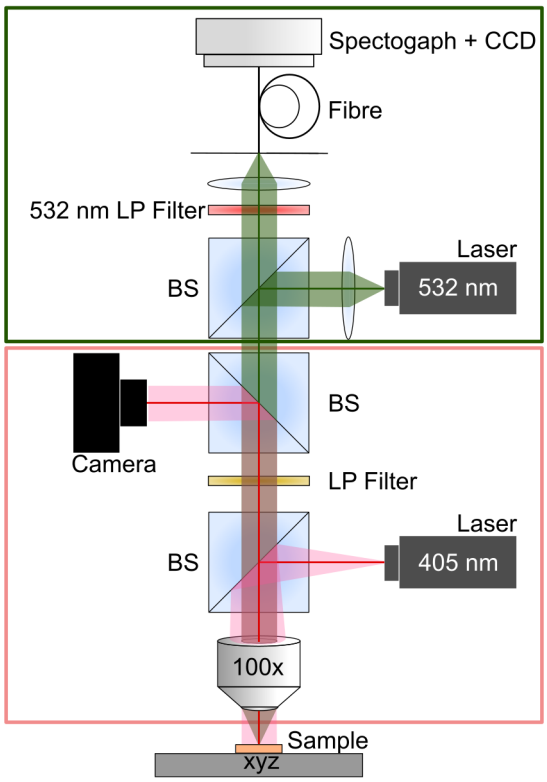

Figure 3.2: Schematic of the WiTec microscope with the Raman configuration (green) working in dark-field mode and the wide-field photoluminescence configuration (red) working in bright-field mode. The moving of the sample and subsequent mapping is possible thanks to the piezo stage (labelled as xyz), which permits the movement in x-, y-, and z-directions. CCD refers to a charge-coupled device, BS refers to a beamsplitter, and LP refers to a long-pass filter.

toluminescence. This method provides a spatially resolved image of the sample's photoluminescence, enabling the identification of monolayer locations and the assessment of their quality based on the brightness and uniformity of the observed photoluminescence.

As shown in red in Fig. 3.2, we use a WiTec α300K confocal microscope on bright-field mode, a 100 times Zeiss EC Epiplan–Neofluar (NA = 0.9) microscope objective and a 405 nm fibre-coupled diode laser that sends a planar excitation incident on the sample. We place a long-pass filter before imaging on a camera to prevent capturing any reflected laser light, in addition to the monolayer emission. We stitch together the final image by using a piezo-actuated stage that periodically shifts the diffraction-limited area being imaged to obtain a larger cohesive image.

To image the heterobilayer, we use two different long-pass filters in combination with two distinct cameras. For WS_2, we use a 600 nm long-pass filter alongside the WiTec's integrated camera. This filter blocks reflected laser light, which has a wavelength below the cutoff, while transmitting the photoluminescence from WS_2 excitons (λ = 620 nm), ensuring that WS_2 is selectively imaged. For WSe_2, we use a 700 nm long-pass filter in conjunction with a 14-bit CMOS camera (Zeiss Axiocam 705 mono). The higher cutoff wavelength suppresses any signal from WS_2, guaranteeing the sole detection of WSe_2. The CMOS camera is selected due to its higher sensitivity, which allows for the detection of the lower emissive power produced by WSe_2. Nevertheless, the WiTec integrated camera remains essential for spatial mapping and vignetting, as it utilises a piezoelectric stage to automatically stitch together images, whereas the CMOS currently relies solely on manual operation.

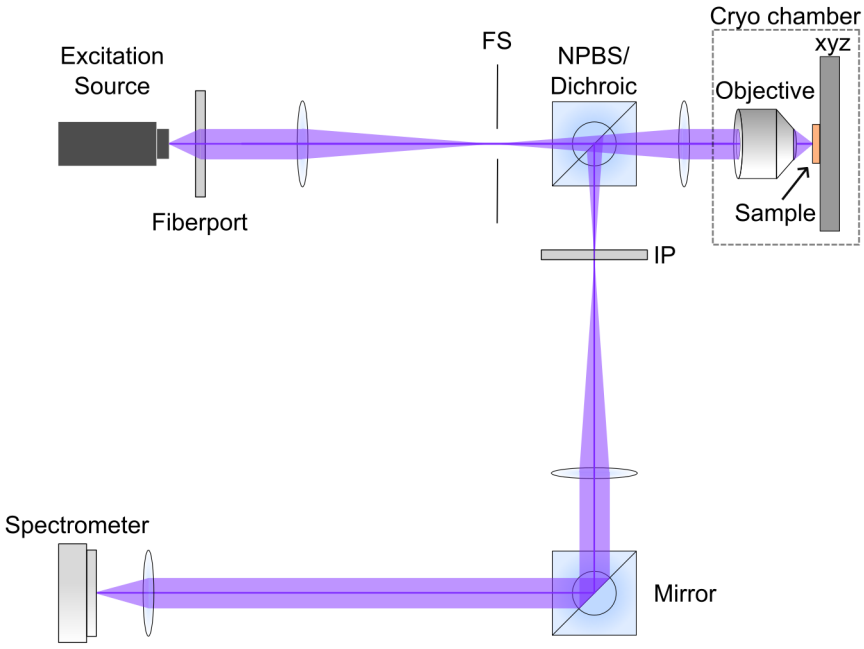

Figure 3.3: Schematic of the Montana cryostat as used for PL with a laser diode as the excitation source. For reflectivity, the laser diode is replaced by a halogen lamp, and an additional lens is added between the fiberport and the first lens. The objective that focuses the incoming laser onto the sample, the piezo stage (labelled as xyz), and the sample are all contained within the cryogenic chamber. FS, NPBS, and IP are acronyms for field stop, non-polarising beamsplitter, and image plane, respectively.

3.2.3 Temperature-dependent Photoluminescence Spectroscopy

This temperature-dependent measurement is crucial for understanding how the optical properties of TMDCs change with temperature. In particular, these measurements allow us insight into the exciton behaviour and the effect of non-radiative recombination on the material. This is particularly significant for interlayer excitons, since they, as a result of weaker binding energies, are less stable at room temperature. However, at low temperatures, they become more stable and intense due to lower thermal energy and non-radiative recombination [36], allowing us to examine their characteristics more clearly.

The sample is placed into a Montana CryoAdvance by mounting it on a sample holder that is surrounded by a heat shield and vacuum chamber, which are contained within the cryogenic chamber box in Fig. 3.3. As such, we place the sample under high pressure and low temperatures to probe the material, using a 504 nm laser, at temperatures ranging from 3 K to 100 K. Apart from differences in temperature and pressure, the temperature-dependent setup works under the same principles as in room-temperature PL. First, an incident laser reaches the material and excites an electron above the valence band to a higher energy state. Then, the electron relaxes back to the valence band, recombining with a hole, causing a photoluminescent emission. The emission passes through a dichroic mirror, which filters out the laser light, and is finally detected in a spectrometer (SpectraPro HRS-300).

3.3 Reflectivity

We measure reflectivity to observe how much incoming light the 2D materials could reflect and, inversely, how much they absorb. Reflectivity is defined as the ratio of the reflected intensity to the incident intensity such that:

$$R(\lambda) = \frac{I_r(\lambda)}{I_i(\lambda)}, \tag{3.1}$$

where incident intensity is I_i, and reflected intensity is I_r.

To accurately measure a sample's reflectivity, it is necessary to take multiple measurements on the sample. The number of measurements needed depends on whether we want to calculate absolute or differential reflectivity. Absolute reflectivity measures the total reflected power and therefore requires a reference with a known reflectivity, like a silver mirror, to be able to make an absolute comparison with our sample. However, the sample with known reflectivity can be substituted by the substrate if the material's reflectance coefficient, R, is known. This results in a new reflectivity ratio of:

$$R_{\text{abs}}(\lambda) = \frac{I_{\text{sample}}(\lambda) - I_{\text{dark}}}{I_{\text{ref}}(\lambda) - I_{\text{dark}}} \cdot R, \tag{3.2}$$

where I_{sample}, I_{ref}, and I_{dark} are the sample's intensity response as a function of wavelength, the reference's intensity response as a function of wavelength, and the dark counts, respectively. In contrast, differential reflectivity only measures the relative change between the reference material and the sample:

$$R_{\text{diff}}(\lambda) = \frac{I_{\text{sample}}(\lambda) - I_{\text{ref}}(\lambda)}{I_{\text{ref}}(\lambda)}. \tag{3.3}$$

In this investigation, the reflectivity is measured using two different setups. The first employs the setup shown in Fig. 3.2 with a halogen lamp (Zeiss HAL 100) replacing the 405 nm laser and a 20 times Zeiss EC Epiplan-Neofluar microscope objective. The camera and any long-pass filters are removed to allow all reflected light to be detected on the WiTec UHUTS300 SMFC VIS Spectrograph (150 grooves/mm). The illumination intensity of the halogen lamp is set to 80%, and both the field stop and the aperture in front of the halogen lamp are entirely closed to limit the range of incident angles to approximate normal incidence. The second setup, shown in Fig, 3.3, measures the reflectivity at different temperatures. The only differences are that the excitation source is a halogen lamp (ThorLabs OSL Fiber Illumination), and an additional lens placed between the fiberport and the first lens.

3.4 Current-Voltage Measurements

Current-Voltage (IV) measurements are crucial in PV research to characterise the electrical response of devices and obtain figures of merit, such as the power conversion efficiency [7]. In these measurements, we apply a voltage sweep across the device using a source-measurement unit (SMU) and record the resulting current. The relationship between current and voltage allows us to identify the device types and calculate other parameters, such as the maximum power.

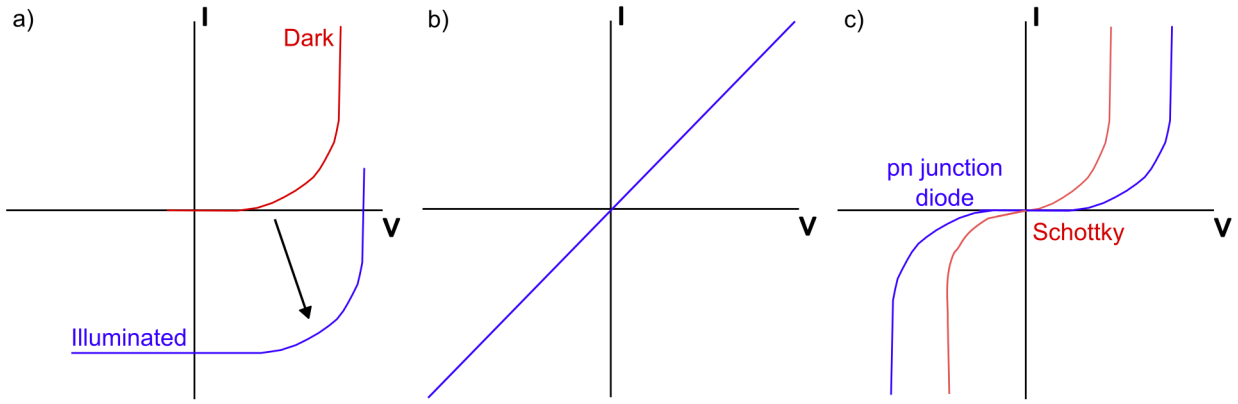

Figure 3.4: Illustration of the IV curves for different types of devices. a) Photovoltaic devices with the curve resting on the horizontal axis indicating a PV under no illumination and the shifted curve indicating a PV under illuminated conditions. b) Ohmic devices. c) Schottky devices (red) and pn junction diodes (blue).

The first type is photovoltaic devices that typically produce negligible current until a threshold voltage is reached, afterwards their current increases exponentially (Fig. 3.4a). The threshold, or "knee", corresponds to the voltage at

which the depletion region formed at the junction narrows and hence, facilitates current production [7]. Under dark conditions (absence of incident light), the current arises from the material's intrinsic properties, resulting in positive current flow. When illuminated, however, the IV curve shifts downwards due to the photoelectric effect inducing photocurrent generation [37], indicating power generation rather than consumption.

In contrast, ohmic devices are unresponsive to light, such that their characteristic IV curve remains unchanged under illumination. Their current-voltage relationship can be defined by Ohm's law:

$$V = IR, \tag{3.4}$$

where V is the voltage, I is the current, and R is the resistance. The linear, symmetric trend shown in Fig. 3.4b) is a result of the lack of a junction or asymmetric energy barrier, which permits electrons to flow unimpeded in either direction [9] and making their response illumination-independent.

The third class discussed are Schottky devices, which are named after the thin Schottky barrier formed at the interface between a metal and a semiconductor. The barrier is a result of the difference in their work functions and electron affinities, which induces the semiconductor's Fermi level to lower to match the metal [7]. The effect of the barrier is indicated by the lower threshold voltage shown in Fig. 3.4c), which results from the thinner Schottky barrier. They also exhibit a similar exponential current increase, similar to PV devices, which occurs as more carriers overcome the energy barrier and contribute to current generation [37]. Regrettably, apart from generating favourable forward-bias currents, Schottky devices experience reverse leakage currents and reduced breakdown voltages under reverse bias, which could permanently damage the cell [7].

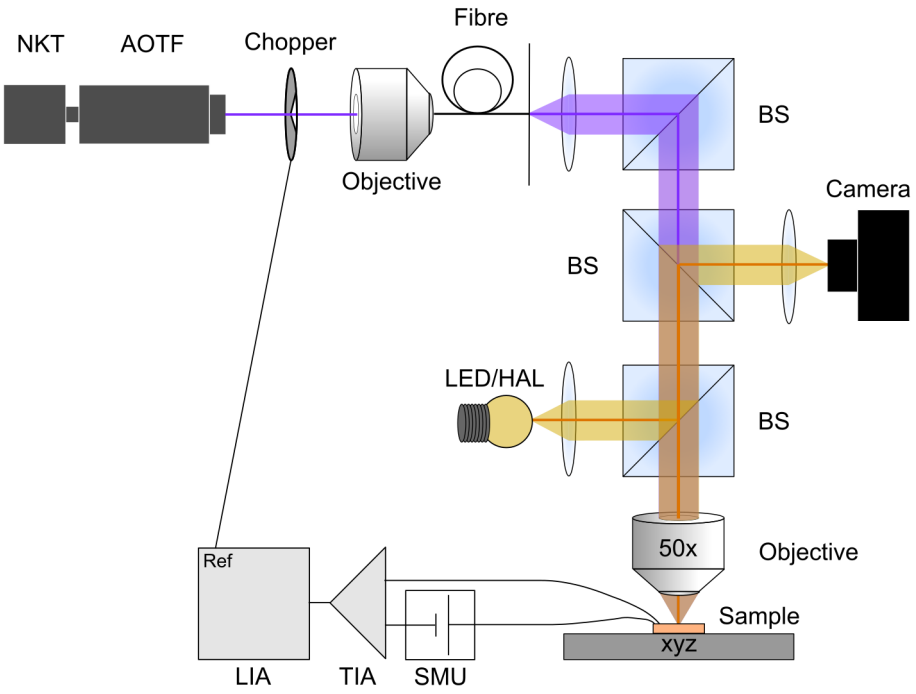

Figure 3.5: Schematic for electronic response measurements. The setup for current-voltage (IV) measurements is indicated with an orange beam path, while the purple beam path indicates the setup for external quantum yield (EQE) measurements. BS corresponds to a beamsplitter, HAL corresponds to a halogen lamp, SMU corresponds to a source measurement unit, TIA corresponds to a trans-impedance amplifier, and LIA corresponds to a lock-in amplifier. Both the LIA and TIA are unnecessary for IV measurements, such that both electrodes from the printed circuit board are connected to the SMU.

To characterise the current response of our device, we employ the setup illustrated in Fig. 3.5 (highlighted in yellow). In the measurement, a light source, either an LED (WiTec integrated) or a halogen lamp (Zeiss HAL 100), is focused onto the sample through a 50 times Zeiss EC Epiplan – Neofluan (NA = 0.55) long-working-distance microscope

objective. We limit the area imaged onto the WiTec's integrated CCD camera by closing the field stop. The sample, mounted on a printed circuit board (PCB), is connected to a Keithley 2600 series SMU via the positive and negative terminals. The SMU send a voltage sweep through the positive terminal and the resulting current returns via the negative terminal to be measured.

3.5 External Quantum Yield

External quantum yield (EQE) is a measure of the fraction of incident photons converted into collected electrons:

$$\mathrm{EQE} = \frac{\text{collected electrons}}{\text{incident photons}}. \tag{3.5}$$

In the ideal device, the EQE equals 1 [38], such that every incident photon generates an electron-hole pair that successfully diffuses to the contacts to produce current as illustrated in Fig. 3.6a). This behavior results in an EQE resembling a step-function (Fig. 3.6b) with the step corresponding to the device bandgap. However, this situation neglects the inevitable losses, resulting from mechanism such as reflection and transmission, that plague practical devices and reduce the fraction of photons absorbed. Moreover, the diffusion length of a material limits the travel distance of electrons, increasing the probability of recombination before reaching the contacts [38]. Hence, in a good, realistic PV device, the EQE transforms into a wavelength-dependent curve as shown in Fig. 3.6b).

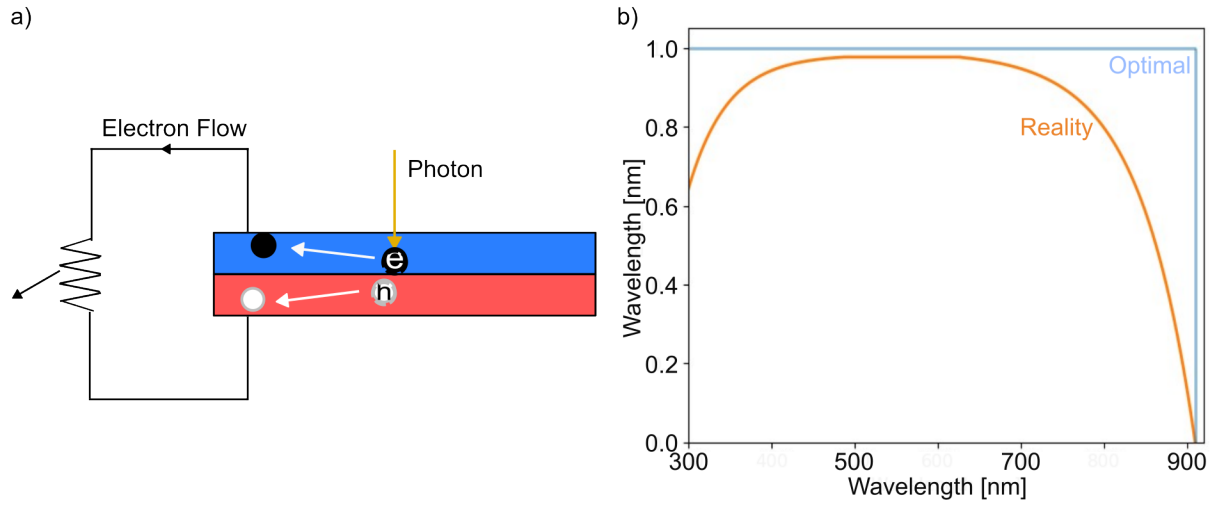

Figure 3.6: a) Illustration showing the case that produces an ideal external quantum efficiency (EQE) in a device: an incident photon results in one collected electron. b) The accompanying EQE plot showing the EQE response as a function of wavelength for the optimal case (blue) and a realistic situation for good quality photovoltaics (orange), taking into consideration expected losses.

Extraction of the EQE requires two separate measurements: the wavelength-dependent photocurrent response of the device under a fixed bias, and the power spectrum of the excitation source used. This is because EQE is more precisely defined as:

$$\mathrm{EQE} = \frac{I_{\mathrm{ph}}(\lambda) \cdot h \cdot c}{q \cdot P_{\mathrm{in}}(\lambda) \cdot \lambda}, \tag{3.6}$$

where h is Planck's constant, c is the speed of light. q is the elementary charge, λ is the wavelength. $I_{\mathrm{ph}}(\lambda)$ and $P_{\mathrm{in}}(\lambda)$ indicate the wavelength-dependent photogenerated current and incident laser power, respectively.

To measure $I_{\mathrm{ph}}(\lambda)$, we utilise the setup indicated by the purple beam in Fig. 3.5. Here, a femtosecond pulse is generated by a supercontinuum white light laser (NKT SuperK Extreme) that passes through an Acousto-Optic Tunable Filter (NKT SuperK Select AOTF), enabling the selection of specific wavelengths. The laser output then passes

through a mechanical chopper (SRS SR640 Chopper Controller) operating at 139.77 Hz, which also acts as the reference frequency for the lock-in amplifier. The chopper is essential for improving the signal-to-noise ratio of our measurement by converting the photocurrent signal from DC to AC and thus removing any unnecessary noise.

The modulated beam is now coupled into a fibre connected to a 50 times Zeiss EC Epiplan – Neofluan (NA = 0.55) long-working-distance microscope objective, before being focused onto the sample. We bias the device, wire-bonded onto a PCB, using a SMU (Keithley 2600 series that applies a voltage of 10 V. The photocurrent returns into the SMU, which is connected to a trans-impedance amplifier (SRS SR570) and a lock-in amplifier (SRS SR830 DSP) to amplify the signal and convert the current into a voltage signal. Then, we remove the electrical measurement components to measure $P_{\text{in}}(\lambda)$ using a ThorLabs PM16-122 power meter. For both measurements, the NKT AOTF cycles through the same wavelength range to ensure consistency between the results.

Having described the optical and electrical spectroscopy methods and established their respective experimental setups used in this thesis, we now introduce the large-area transfer method developed for manipulating large-area monolayers. These methods will continue to be used in subsequent chapters to probe WS_2/WSe_2 heterostructures, allowing for a detailed investigation of the heterostructure composition, the intralayer and interlayer excitonic interactions, and their temperature-dependent optical responses. Overall, these techniques contribute to the systematic investigation into the optoelectronic properties of TMDC systems.

Chapter 4

Development of Large-Area 2D Material Transfer

In this chapter, we discuss the techniques used for exfoliation and transfer of large-area 2D materials. Firstly, we explain the established gold-assisted exfoliation method [39] used to achieve large-area monolayers (4.1). Then, we explore the large-area stamping method developed for their transfer to different substrates (4.2). This involves examining the materials involved in the transfer, their interaction with monolayers, and the procedure itself. Finally, we also briefly discuss the additional uses of large-area stamping (4.3) and some limitations of the large-area transfer method (4.4).

4.1 Gold-Assisted Exfoliation

The fabrication of TMDC monolayers can be categorised into two types: top-down fabrication and bottom-up fabrication, each with distinct advantages and disadvantages. Within the field of TMDCs for photovoltaics, these groupings can be further reduced into two main fabrication methods: mechanical exfoliation, top-down, and chemical vapour deposition, bottom-up. Early demonstrations of PV used small exfoliated flakes [25] because mechanical exfoliation returns good quality, monocrystalline monolayers as long as the initial crystal is of good quality. However, devices made using this method are limited to dozens of micrometers [9] , which makes large-scale production of TMDC PVs impossible with this method.

In contrast, CVD as a bottom-up fabrication method is more compatible with the scaling up required for commercialisation as it produces cm-scale monolayers [9]. However, in addition to the high temperatures required, it is based on the homogeneous nucleation and growth of atoms into TMDC monolayers impacted by a number of variables such as the vapour precursors, substrate type and structure, pressure, and flow rate [40]. This means that, although the quality of CVD-grown monolayers has improved significantly, it is still prone to producing polycrystalline layers with inhomogeneous surfaces [8], resulting in more defects and hence weaker light-matter interactions. The ideal fabrication method would combine their respective advantages of producing a) large areas and b) monocrystalline monolayers. Hence, we utilise Au-assisted exfoliation, which can produce mm-sized high-quality monolayers [39], to exfoliate our TMDC monolayers from bulk crystals.

We begin by using Nitto tape (SPV-224) to cleave bulk WS_2 and WSe_2 crystals (HQ Graphene) into smaller crystals. After cleaving the crystal a couple of times, a much thinner and cleaner interface is exposed from which we can exfoliate monolayers. The process for exfoliating large-area monolayers using GAE is shown in Fig. 4.1a). First, obtaining a monolayer from our previously cleaved crystal requires the use of ~100 nm of atomically flat gold deposited onto a pristine silicon wafer. On top of the gold lies a ~300 nm poly(methyl methacrylate) (PMMA) resist layer spin-coated for additional rigidity. We strip the gold using thermal release tape (Nitto RA95LS), which is pressed onto the wafer and then carefully peeled off. This creates a Au, PMMA, and thermal release tape (TRT) stack, which is pressed onto the recently cleaved TMDC crystal, allowing exfoliation of a monolayer onto the gold surface. Figure 4.1b) shows an example of WS_2 monolayer exfoliated onto the gold with a scale on the order of hundreds of micrometres. The high monolayer exfoliation success rate observed with this method is attributed to the strong binding between gold and a 2D monolayer, which overcomes the weaker interlayer binding in the bulk crystal [39]. Once exfoliated, the Au/PMMA/TRT stack containing the monolayer is transferred onto a clean silica (SiO_2) substrate, resulting in a

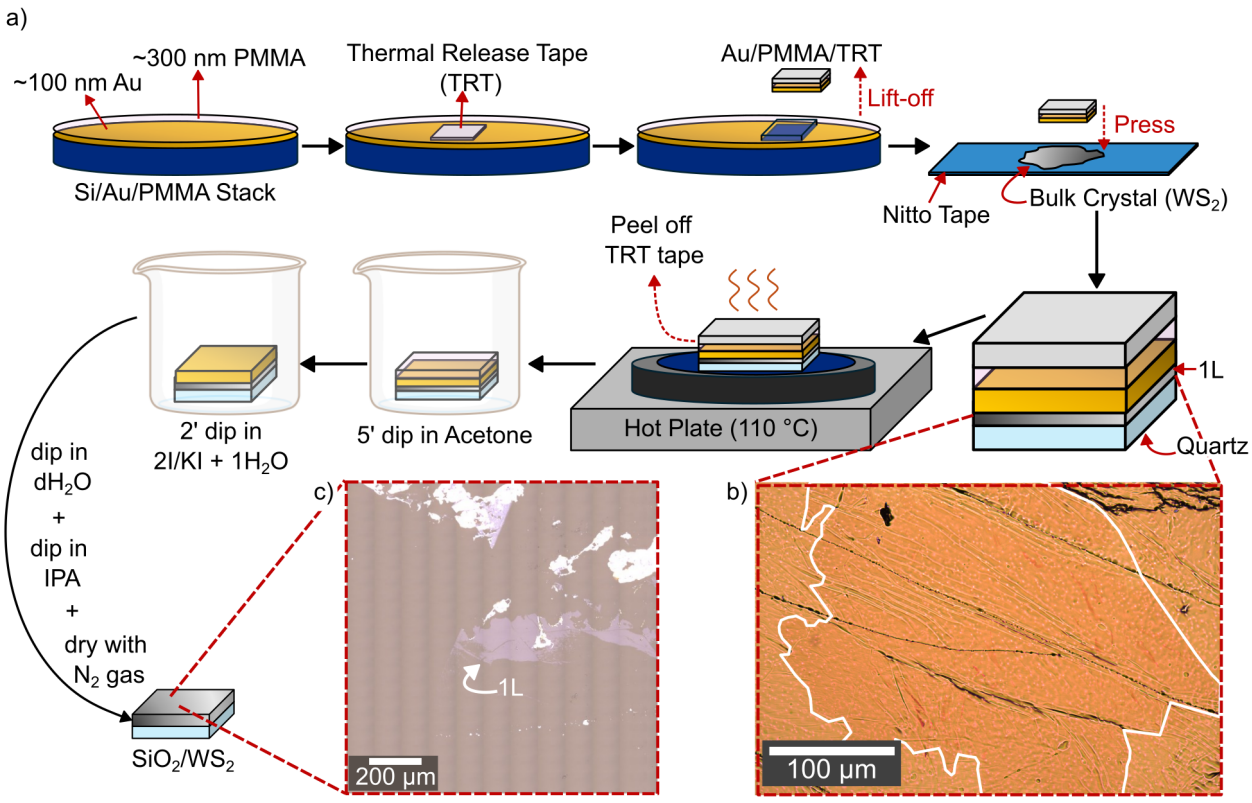

Figure 4.1: a) Gold-assisted exfoliation procedure to produce a TMDC monolayer. The images show WS_2 on b) the Au/PMMA/TRT stack and c) after etching the gold and cleaning the substrate. The monolayer in b) is highlighted by a white border, while the monolayer in c) is indicated by an arrow.

SiO_2, monolayer, PMMA, gold, and TRT stack.

The next step is to etch the gold and clean the substrate, leaving only the monolayer on the substrate. The first step involves heating the substrate on a hot plate (IKA RCT Basic) to 110 °C to remove the TRT, which has a release temperature of 90 °C. The sample is then dipped into a beaker filled with acetone for five minutes to remove the PMMA (resist) from the gold. Afterwards, using Teflon tweezers, the substrate is quickly dipped in isopropanol (IPA) before being transferred to a small Petri dish filled with one part distilled water (dH_2O) to two parts mild gold etchant solution (KI/I_2). Here, the IPA pre-dip is intended to slow the etching effect of the etchant solution on the gold, thereby removing the gold without also removing the monolayer. Using the same Teflon tweezers, we dip the sample into the etchant solution and gently stir the substrates continuously for two minutes. After etching the gold, we pass the substrate through dH_2O, followed by clean IPA to completely remove any leftover etchant or gold remaining on the substrate. Finally, once clean, the substrate is dried with a N_2 gun. The outcome is shown in Fig. 4.1c). While GAE can also collect some bulk material, it reliably produces monolayers that are hundreds of micrometres wide, an improvement on monolayer sizes produced using mechanical exfoliation, that are suitable for large-area stamping..

4.2 Large-Area Stamping - Single Monolayer Transfer

4.2.1 Stamp Fabrication

The primary material involved in the stamp (and stamping procedure) is LDPE. However, as shown in Fig. 4.2, the stamp fabrication entails the use of additional materials to achieve the desired transfer. The base of the stamp is a

glass or SiO_2 square substrate on which a thin square of polydimethylsiloxane (PDMS) is placed to provide additional distance between the substrate and the superglue drop. On top of that lies a thicker but smaller square of PDMS, which limits the expansion of the superglue drop due to the edges generating a pinning force [41]. Once the PDMS squares are stacked onto the base, a drop of superglue is placed on top of the thick PDMS and left to air dry for a day to ensure its rigidity. The dried superglue plays an imperative role as a guide through which to align with our monolayer. Altogether, the components form a stable base onto which we can place the LDPE, and later align it with our monolayer, enabling precise material transfers.

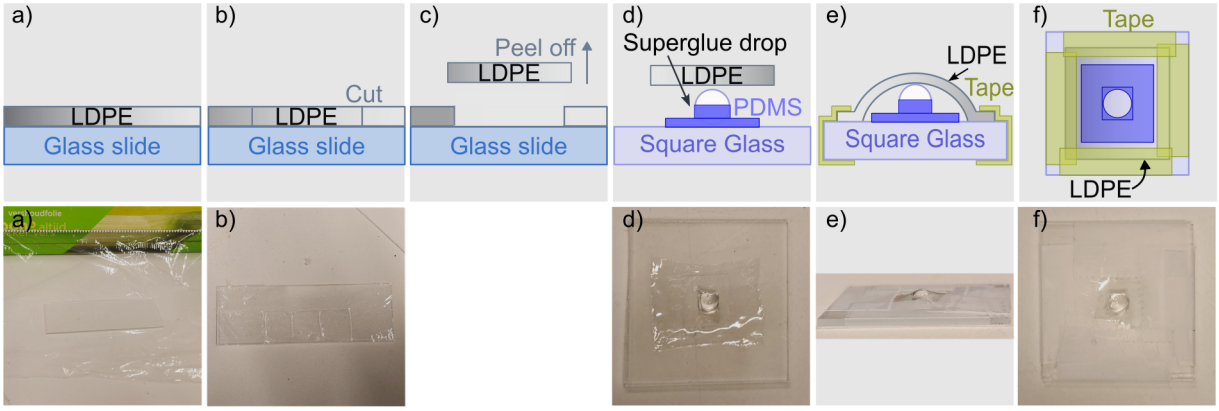

Figure 4.2: Illustrations (top row) accompanied by images (bottom row) showing the actual process of adding LDPE to our stamp for 2D material transfer. a) shows the stretching of LDPE on a slide. b) shows the cutting of LDPE squares from the stretched LDPE. c) shows the peeling of the LDPE square. No image equivalent of this step was taken; as such, the space is left blank. d) shows the flipped LDPE being placed on the already dried superglue. e) and f) show the final stamp from the side and top, respectively.

To complete the stamp assembly, the LDPE film is carefully prepared and attached to the base mentioned above. First, as shown in Fig. 4.2a) and b), we obtain the square of LDPE used on a stamp by cutting out from a piece of LDPE that we stretch and smooth out on top of a microscope slide. Next, we cut the piece such that the resulting square is smaller than the substrate and flip the peeled LDPE square over so that the unexposed, clean surface is now facing outwards as shown in Fig. 4.2c). The LDPE is finally taped so that the LDPE is stretched tightly across the glue drop as depicted in Fig. 4.2e) and 4.2f). The smooth and clean interface plays a crucial role in achieving a consistent monolayer pickup, a vital step in our large-area transfer method.

4.2.2 Monolayer Transfer

The large-area transfer of 2D materials can be divided into two distinct sections: pickup and release. These sections are then further subdivided into contact, lift-off, and drag as illustrated in Fig. 4.3a).

The transfer begins with the pickup, specifically the contact step, which consists of lowering our stamp at a speed of 500 nm/s and an acceleration of 0.01 mm/s² using a piezoelectric controller. The controlled speed ensures that initial contact between the LDPE and the monolayer (shown in Fig. 4.3b) occurs gently and slowly at the bottom of the superglue drop. This initial contact is performed at a temperature of 70 °C. Once the contact with the desired monolayer area is established, the stamp (and by proxy the monolayer) is heated above the LDPE melting point (118 °[42]) using a copper heating stage controlled by an Enda ET2011 PIB temperature controller to reach the target temperature of 140 °C. At this temperature, LDPE softens and transitions from a solid to a liquid state, allowing it to conform to the monolayer. Furthermore, the melted LDPE also enhances the adhesion with the monolayer surface as a result of mechanically interlocking onto irregularities [43].

With the monolayer encapsulated by the melted LDPE, the lift begins by cooling the LDPE back to 70 °C so that the LDPE solidifies while still maintaining strong contact with the monolayer. Once the LDPE has solidified, we lift the stamp with a speed of 500 nm/s and an acceleration of 0.01 mm/s^2 and, as a consequence, also pick up the monolayer

underneath, as shown in Fig. 4.3c).

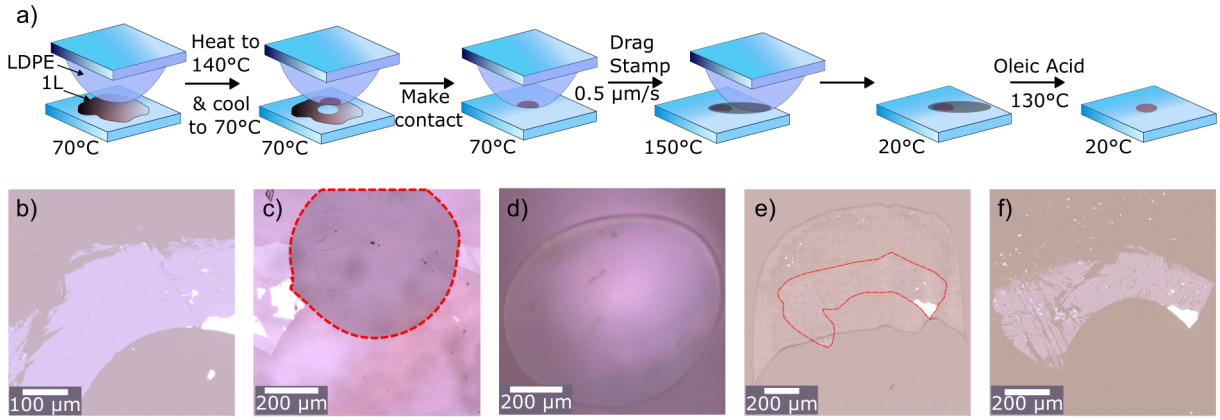

Figure 4.3: Illustration of the stamping procedure, a), and the corresponding images b)-f). b) shows the substrate after Au-assisted exfoliation but before transfer. c) shows the substrate after monolayer pickup with the red line indicating the contact spot between the stamp and the substrate, as well as the 1L removed. d) shows a microscope image of the stamp after pick up, with the monolayer being shown as a darker shade on the image. e) shows the monolayer (encased in red) below the solidified LDPE that remains after dragging. f) shows the 1L after cleaning in oleic acid (OA) at 130 °C for 30 minutes.

Having successfully picked up the monolayer that now resides on the stamp as shown in Fig. 4.3d), the last stage is to release the monolayer. Before starting, however, we clean the substrate by placing it under 2 minutes of air plasma to remove any organic contaminants and water vapour, which can interfere with the deposition of our monolayer. The first step involves bringing the stamp into contact with the cleaned substrate using the same speed, acceleration, and temperature as during the initial pickup. The controlled descent of the stamp is maintained until the edge of the LDPE extends beyond the end of the monolayer. Afterwards, the descent is stopped and the copper stage is heated to 150 °C to decrease the viscosity of our LDPE, causing a reduction in the friction experienced at the monolayer-LDPE interface [44]. This ensures that, during the last step involving dragging (performed at 500 nm/s), the monolayers remain attached to the substrate. Finally, after the stamp has moved past the monolayer, we lift it at a speed and acceleration of 2 mm/s and 2 mm/s², and allow the substrate to cool back to room temperature, which completes the transfer process.

However, some melted LDPE remains on the monolayer and eventually re-solidifies as shown in Fig. 4.3e), and must be removed to obtain clean interfaces. The removal is accomplished using oleic acid (OA), a weak acid. On a hot plate, the substrate and a small Petri dish filled with OA are heated simultaneously to 130 °C. This simultaneous heating minimises the thermal shock experienced by the substrate, while also melting the LDPE and increasing the likelihood of removal. Once at 130 °C, the substrate is quickly placed in the Petri dish, covered, and left for 30 minutes. Afterwards, the substrate is rinsed in IPA until clean to remove any remaining OA and then dried using a N_2 gun. The result is a large-area LDPE-free monolayer that was successfully transferred using LDPE and cleaned using oleic acid as shown in Fig. 4.3f).

4.2.3 Effect of LDPE and Oleic Acid on Large-Area Stamping

Following the successful LDPE-based monolayer transfer, it is important to briefly discuss the justification of choosing LDPE over other polymer films. As mentioned previously, LDPE is a critical component for large-area transfer due to its ability to conform to the monolayer and create mechanical interlocking. Additionally, LDPE is safer and more practical than alternative polymer films considered. One of these alternatives considered was polyvinyl chloride (PVC), which posed two significant disadvantages: it has a higher melting temperature [45] and emits hydrogen chloride when heated above 135 °C [46]. LDPE, by contrast, commonly known as kitchen cling film, is cost-effective and readily available, which helps simplify the stamping process.

In addition to its practical advantages, as shown in Fig. 4.4a) by the exciton linewidth sharpening, using LDPE improves upon the initial exciton quality of our exfoliated monolayer (Fig. 4.4b and 4.4c). Although the precise mechanism behind this enhancement is not yet fully understood, we suggest the following mechanism. The sharpening of the peak occurs while LDPE still covers the WS_2 as shown in Fig. 4.4d), with the respective wide-field PL image being Fig. 4.4e). Hence, the decrease in the exciton linewidth may be caused by LDPE being a chemically resistant material [47], passivating the monolayer surface and protecting it from interacting with environmental adsorbates.

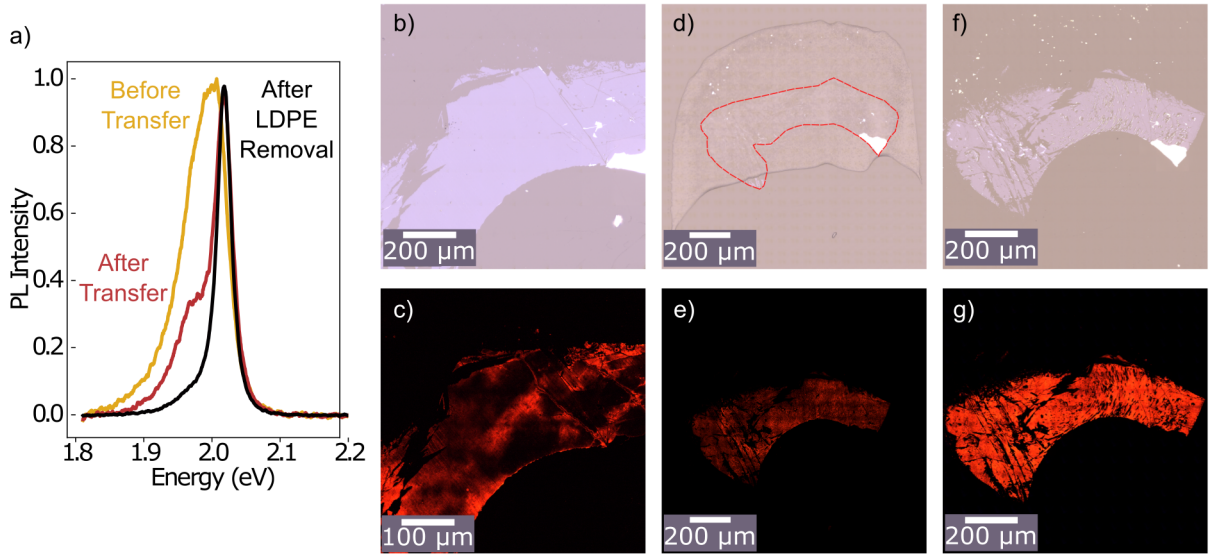

Figure 4.4: A normalised PL plot showing sharpening of the exciton peak from 37 meV before transfer to immediately after transfer, and finally to an exciton peak with a linewidth of 27 meV after LDPE removal with OA. b) – g) Bright-field and wide-field PL microscope images taken through the course of WS_2 transfer: from the monolayer after exfoliation, b) and c), to the monolayer immediately after transfer with LDPE still on top, d) and e), and ending with the monolayer after LDPE removal using OA, f) and g).

Although the LDPE on the monolayer is shown to improve the exciton linewidth, its removal remains critical to obtain clean samples. This proves to be difficult as a result of LDPE's chemically resistant nature. This complicates the search for an easy and efficient LDPE removal method to eliminate the dry LDPE displayed in Fig. 4.4d). Initially, plasma cleaning and vacuum annealing were explored without success, leading to a shift towards a chemical solution.

To facilitate solvent selection, chemical compatibility charts provided by LDPE manufacturers were consulted. These charts indicate which solvents can affect LDPE as well as at which temperature ranges. In particular, LDPE appears to be most reactive to aromatic and halogenated hydrocarbons as well as aromatic ketones, with lesser reactivity to aliphatic hydrocarbons [47]. This is due to the polarity-based solubility principle, where solutes tend to be dissolved by solvents with the same type of polarity. Such is the case for LDPE, a non-polar material [48], which is therefore only affected by all the aforementioned non-polar or weakly polar chemicals.

Furthermore, we also consider the thermal properties of the chemicals to find safe solvents. In particular, we examine the boiling points of the solvents compared to those of LDPE. The purpose is to identify solvents with boiling points and flash points that are significantly higher than the melting point of LDPE. This allows us to soften the LDPE without evaporation or ignition, which could physically damage the monolayer. As a result, commonly cited solvents [49] such as xylene (flash point = ~20 °C [50]) and trichloroethylene (boiling point = ~87 °C [51]) were eliminated from consideration due to their low thermal stability.

With a narrowed candidate list, we evaluate LDPE solubility in toluene (aromatic), chloroform (halogenated), hexane and cyclohexane (aliphatic) at both room temperature and elevated temperatures. These confirmed LDPE's high chemical resistance, as no significant deformation was observed under any condition. This failure led us to consider acids as a potential solution. Particularly, trigluoromethanesulfonimide (TFSI), a superacid, which improves exciton

quality [52]. However, there were two constraints when selecting acids: 1) most acids are polar but LDPE requires non-polar or weakly polar solvents, and 2) strong acids may degrade metal contacts, which is undesirable for device fabrication. However, while TFSI violates the constraints, oleic acid, as a weak acid, causes negligible damage to metal contacts after OA treatment [53]. OA (Fig. 4.5a) also possesses a high boiling point (360 °C [54]) and flash point (189 °C [55]). Finally, OA is proven to improve exciton quality [53, 56, 57], which means that it fulfils all the previously dictated objectives and also enhances the optical properties of the monolayer.

After identifying OA as a suitable candidate, we found that heating it to 130 °C enables its removal as outlined in 4.2.2. This may result from a couple of effects. Although the exact removal mechanism has not been explored, we propose two possible explanations. First, as both are non-polar chemicals [55], OA can intercalate within LDPE and help soften it even further. Secondly, OA may decreases LDPE's mechanical strength and adhesion since, as OA intercalates between the chains in LDPE, it acts like a plasticiser and weakens the intermolecular forces [58]. So, rather than completely dissolving the LDPE through a physical reaction, the OA may also facilitate the separation of it from the monolayer and substrate to obtain a monolayer that resembles the monolayer in Fig. 4.4f).

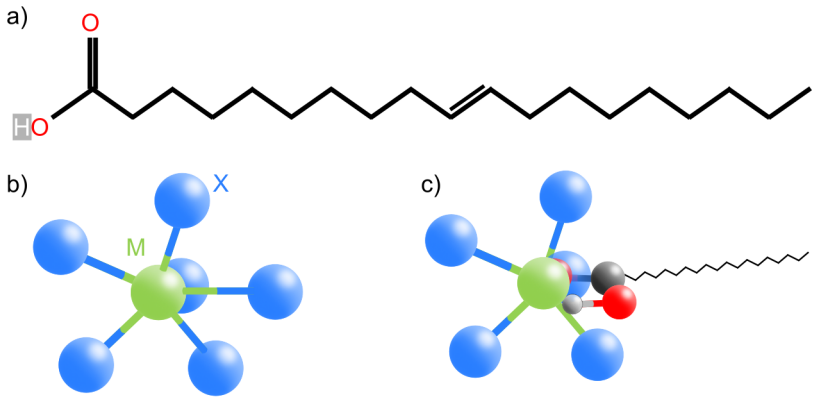

Figure 4.5: Illustrations of a) the skeletal structure of oleic acid, b) the typical unit cell of a TMDC monolayer with one transition metal surrounded by six group 6 (chalcogenide) atoms, and c) a TMDC monolayer with a chalcogenide vacancy, which is passivated by the oxygen substitution provided by the carboxyl acid moiety in OA.

Examining the shift exhibited by the PL spectrum in Fig. 4.4a) from beginning (before transfer) to end (after LDPE removal), the exciton linewidth narrows from 37 to 27 meV and reaches values close to those obtained with traditional mechanical exfoliation (4.1). This agrees with the previously documented effect of OA on TMDC monolayers. This effect is further enhanced after comparing the transition between the wide-field PLs shown in Fig. 4.4b), 4.4d), and 4.4g). Each consequent step produces a more homogenous photoluminescence, with the initial monolayer showing many PL-deficient areas (Fig. 4.4b) and the highest uniformity occurring after OA treatment Fig. 4.4g).

As illustrated in Fig. 4.5b), a pristine TMDC unit cell is composed of a transition metal atom bonded to six chalcogen atoms, however TMDCs often have chalcogen (S) vacancies. The OA treatment enhances photoluminescence by healing these vacancies and removing defect states through the replacement of chalcogen atoms with oxygen atoms from its carboxyl moiety [57], as illustrated in Fig. 4.5c). The reduction in vacancies and trap states induces a narrowing in the linewidth because of the decrease in non-radiative recombination and trion suppression [53]. The trion suppression is evident when comparing the shoulder in the "Before Transfer" spectrum with the "After LDPE Removal" spectrum shown in Fig. 4.4a). While the shoulder indicates the presence of two Lorentzian peaks corresponding to the neutral exciton at 2.00 eV and the trion at 1.95 eV, the PL after LDPE removal shows one singular peak centred at 2.00 eV, which corresponds to the neutral exciton. The long alkyl tail on OA is also suggested, though not proven, to enhance the neutral exciton PL observed by acting as an encapsulant. Resembling the effect of OA on quantum dots, the tail of OA protrudes from the surface and acts as a barrier against atmospheric reactants that affect the quality of our monolayer [53]. Having discussed the beneficial impact of LDPE and OA, the next step is to explore the additional capabilities of large-area stamping.

4.3 Additional Uses of Large-Area Stamping

Beyond transferring large-area individual monolayers between flat substrates while also improving their excitonic quality, this large-area transfer method also permits us to transfer onto a variety of other surfaces with varied profiles. Of particular interest for this project is the ability to transfer multiple monolayers onto a substrate with contacts to fabricate heterostructure devices, as discussed in Chapter 6. Moreover, the method can also successfully transfer monolayers onto surfaces covered with nanoholes, such that the monolayer partially conforms to the holes and drapes over them. This conformation allows us to image the nanoholes via wide-field PL, whereas before transfer, even high-magnification microscopy using a 100 times Zeiss EC Epiplan–Neofluar (NA = 0.9) microscope objective failed to resolve them. This technique is also useful for substrates with inhomogeneous surface roughness, such as diffusers, where the roughness would typically cause the monolayer to rupture completely. Instead, this technique yields a largely intact monolayer, demonstrating the flexibility of monolayer transfer using this large-area stamping method.

In addition to monolayers, the large-area transfer method also facilitates the transfer of individual hexagonal boron nitride (hBN) flakes and hBN/monolayer stacks onto substrates with diverse levels of surface adhesion. This distinction enables the single-step fabrication of devices encapsulated by hBN. Furthermore, the single-step transfer can successfully stamp hBN/monolayer heterostructures onto a substrate featuring 2.5-μm-high sapphire domes, which have low surface adhesion due to a limited contact area, as well as onto a 50 μm by 50 μm metasurface designed to enhance exciton dampening under TE-polarisation. These demonstrations highlight the versatility of the large-area stamping technique developed, making it a valuable approach for future applications in diverse sample and device fabrication. A more focused exploration of this method and its application range is currently being prepared for publication.

4.4 Current Limitations

While this method is effective in a range of situations, there are a couple of limitations. The most significant concern is humidity sensitivity. In the case of GAE, both high and low relative humidity can affect the monolayer exfoliation yield, with the optimal conditions likely falling between 20–40% RH. Similarly, low humidity also appears to impact the reliability of the 2D large-area pickup. In particular, humidities below 20% RH seem to reduce the transfer efficiency. To address this, environmental conditions can be controlled using a nitrogen purge to reduce humidity or a humidifier to increase it as needed.

Another limitation arises during the monolayer pickup stage, where the pressure exerted by the stamp may lead to the monolayer cracking. This may compromise device performance by having non-continuous regions, which hinder the charge transport and hence, result in an incomplete circuit. Further investigation using pressure sensors could be used to quantify the optimal pressure to preserve monolayer integrity.

Further investigation into the LDPE removal mechanism is also essential for developing a more comprehensive understanding of the transfer procedure. Nevertheless, despite these limitations, the combination of GAE and large-area stamping provides a reliable method for fabricating large-area TMDC heterostructures with good excitonic quality. In the following chapter, this approach is utilised to manufacture a WS_2/WSe_2 heterostructure and to explore the resulting physical and electronic coupling between the layers.

Chapter 5

Optical Characterisation of a 2D Material Heterostructure

In this chapter, we evaluate the optical properties of a WS_2/WSe_2 heterostructure fabricated through sequential use of the large-area monolayer transfer described in Chapter 4. The WS_2, and WSe_2 monolayers are stamped such that there are separate monolayer regions joined by an overlapping region resembling a Venn diagram, as shown in Fig. 5.1a). This characterisation aims to assess whether the transfer process, particularly the use of LDPE and OA, successfully creates clean heterostructures or leaves behind residue that hinders interlayer coupling. This is assessed using three techniques: 1) Raman spectroscopy, which we use to determine physical coupling between monolayers (5.1), 2) PL spectroscopy, which we use to evaluate the electronic coupling as well as probe the intralayer and interlayer properties (5.2)., and 3) reflectivity, which we employ to investigate the interlayer exciton formation mechanism (5.3).

5.1 Raman Spectroscopy and Mapping

Raman spectroscopy is used to probe the physical interaction between the monolayers in our WS_2/WSe_2 heterostructure (5.1b), fabricated using the large-area transfer method introduced in Chapter 4. The physical interaction can be determined by observing the changes in peak intensity or the emergence of new modes. As such, we first identify the characteristic Raman modes of each monolayer. The full Raman spectrum of our HS is shown in Fig. 5.1c), including the corresponding monolayer modes.

For WSe_2, a peak appears at 250 cm^{-1}, which is attributed to the superposition of the A_{1g} and E^1_{2g} modes. The A_{1g} mode is insensitive to the number of layers, as noted in Chapter 3. In contrast, the E_{2g} mode at 350 cm^{-1} is generally insensitive to thickness. The presence of these two peaks enables us to create a map of the HS, shown in 5.1d), by highlighting the regions dominated by each material based on their relative intensities. The resulting map, shown in Fig. 5.1e), indicates the location of each monolayer. Here, it is apparent that WS_2 layer coincides precisely with the region labelled as WS_2 in Fig. 5.1d), while the area marked by the A_{1g} mode also agrees with the region labelled as WSe_2.

A third peak is observed in the Raman spectrum (Fig. 5.1c), which corresponds to another A_{1g} mode that is significantly enhanced in the presence of a WS_2/WSe_2 HS. The effect is likely a result of increased interlayer interactions, which are maximised with certain twist angles and interface quality between the monolayers [59]. The significant enhancement of this A_{1g} peak compared to a WS_2 Raman spectrum suggests a slight twist angle approaching 0° or 60°, where the atomic vibrations align with the interlayer interactions [35]. Therefore, the green region highlighted in Fig. 5.1e) indicates the location of the HS where the WS_2 and WSe_2 are sufficiently overlapping to produce interlayer-enhanced modes.

Additionally, a peak at 309 cm^{-1}, defined as a B_{2g} mode [35], is observed but not marked in the Raman spectrum shown in Fig. 5.1c). This mode appears as a result of interlayer bonding in stacked heterostructures [35]. Although not as pronounced as other modes, its presence still provides supporting evidence for the physical interlayer coupling. However, given its low intensity and high spectral overlap with different peaks, this mode is not included in the Raman map (Fig. 5.1e).

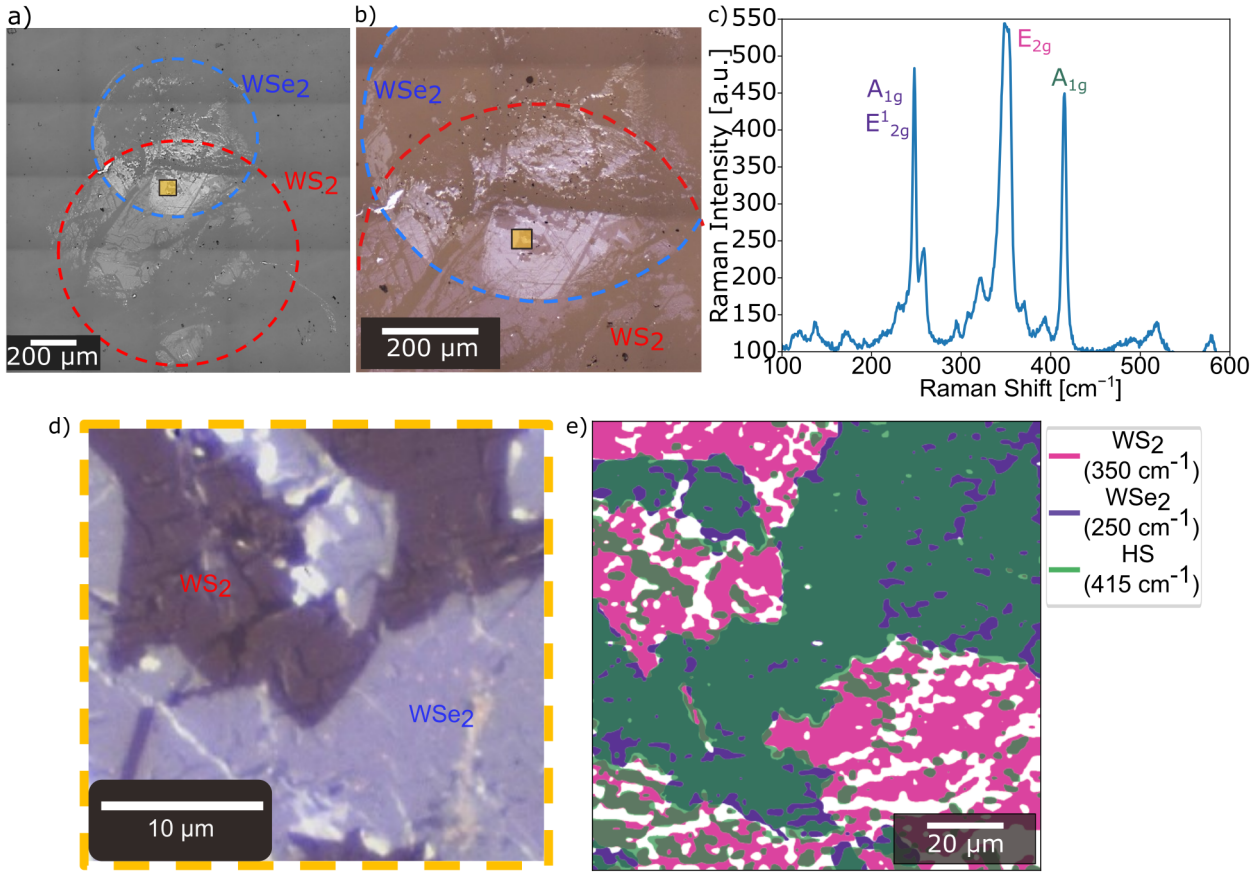

Figure 5.1: Analysis of the WS_2/WSe_2 heterostructure. a) displays the complete monolayer transfer, including the individual monolayers (marked by their respective dotted line), with the heterostructure in the middle. b) shows a close-up of the full heterostructure. The plot c) shows the Raman spectrum measured where both WS_2 and WSe_2 monolayers overlap. The peaks are labelled according to their modes, and the labels are colour-coded to match their respective layers in e). d) explicitly shows the area mapped during Raman and room-temperature PL spectroscopy. The yellow box indicates the location of the mapped area within the heterostructure in a) and b). e) is a 70 μm by 70 μm rotated Raman map of the area shown in c). Each colour represents a different configuration within the heterostructure, indicating the location of the highest intensity peaks.

Altogether, the Raman modes observed in the HS confirm the physical coupling between the WS_2 and WSe_2 monolayers [35, 60]. This suggests that any LDPE or OA residue left after cleaning does not significantly hinder interfacial contact. Furthermore, the map derived from the Raman spectra (Fig. 5.1e) indicates regions of interest for future analysis on the nature of the electronic coupling.

5.2 Photoluminescence Spectroscopy

5.2.1 Room Temperature Photoluminescence Spectroscopy and Mapping

The same HS area mapped in Fig. 5.1a) is also characterised using room temperature PL spectroscopy, as shown in 5.2a). However, unlike Raman spectroscopy, which aids in proving the existence of interfacial contact between WS_2 and WSe_2, PL tests the excitonic response of the HS and thus provides insight into the electronic coupling experienced. Stronger electronic coupling typically indicates a greater wavefunction overlap between electrons and holes residing on opposite layers, which leads to the formation of interlayer excitons.

Interlayer excitons are known to have reduced radiative recombination and longer lifetimes as a result of the increased

separation between electron-hole pairs [10]. Therefore, in particular at room temperature, the PL peaks observed tend to be broader and weaker [10]. As such, prior work emphasises the importance of the twist angle on the stacking alignment in order to be resolve IX at room temperature [20, 22]. In this case, the monolayers were randomly stamped, which produces some uncertainty regarding the presence and visibility of IXs at room temperature.

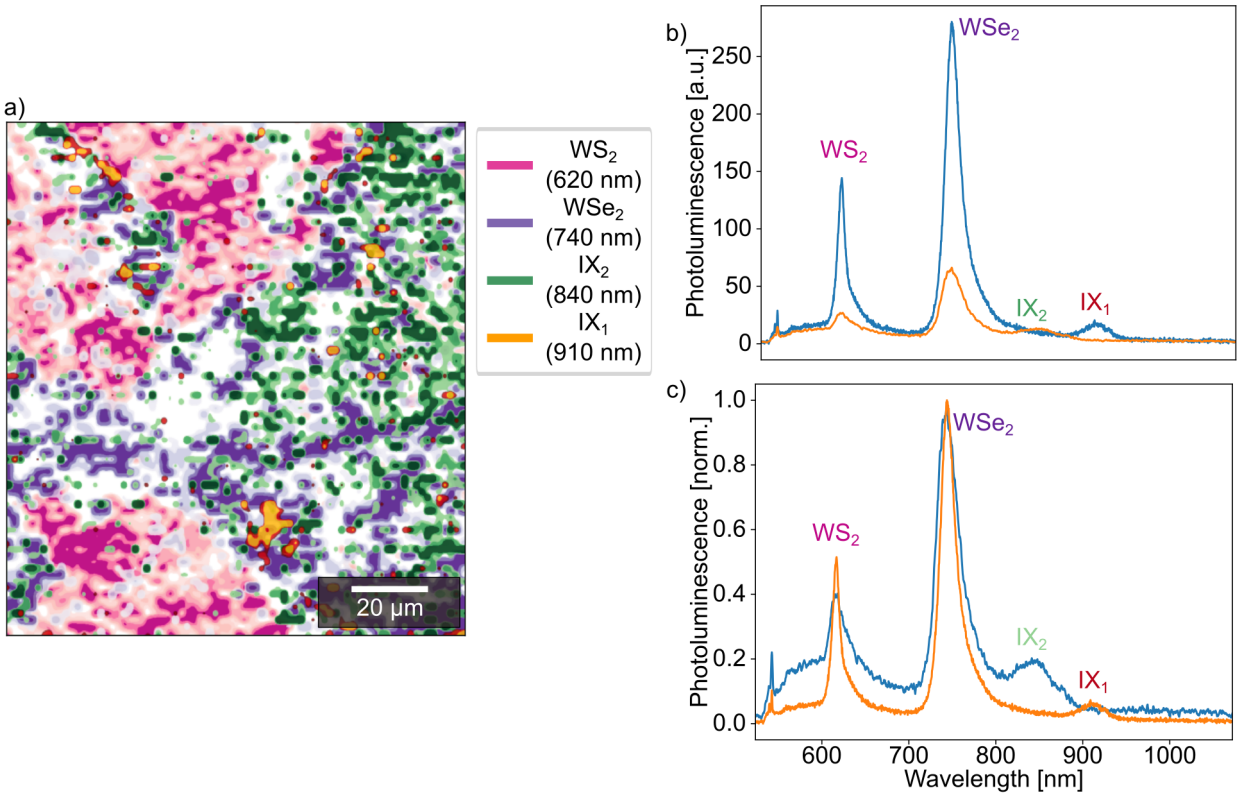

Figure 5.2: a) is the resulting PL map from probing the 70 μm by 70 μm area shown in Fig. 5.1d). The hue of the corresponding colours indicates the intensity measured. b) and c) show two PL spectra taken at different points on the heterostructure. The spectra shown in b) and c) are the same, but c) is normalised for better visualisation of the peaks. The corresponding peaks in the spectra are also colour-coded according to the map colours.

Firstly, we identify the peaks attributed to the individual WS_2 and WSe_2 monolayers. Fig. 5.2b) and 5.2c) show two PL spectra collected at different locations on the HS. Both display three distinct peaks, but only share two across measurements. These correspond to the A-exciton emissions from WS_2 (620 nm) and WSe_2 (740 nm) [61].

The third and fourth peaks, on the other hand, are not present when examining the pure monolayers. One lies at ~910 nm and the other at ~840 nm. The first possibility is that this might be an effect of defect-related emission. However, the WS_2 defect states emit at ranges of ~660 nm [62] while the WSe_2 defects states are detected at ~810 nm [63], which are both offset from both unknown peaks. Hence, we suggest that these peaks correspond with interlayers excitons. The peak at ~840 nm is well-documented to correspond to an interlayer exciton, however it is posited that the peak at ~910 nm also corresponds to a second interlayer exciton [61]. The reduced intensity of the third and fourth peaks relative to the intralayer A-excitons, resulting from their reduced radiative efficiency [10], further supports this hypothesis. As such, for future reference, the 840 and 910 nm peaks are henceforth referred to as IX_2 and IX_1, respectively.

Although these peaks are visible on the room-temperature PL map (Fig. 5.2a), their distribution is more inhomogeneous and scattered than that of the intralayer excitons. This is partially due to only the highest relative intensities being clearly resolved in the original measurements. However, the irregularity of the PL brings us to suggest an additional reason why the IX is scattered: TMDCs are sensitive to physical effects placed upon it, such as strain and twist angle [64, 61].

In particular, the twist angle is frequently discussed as a factor that significantly affects the magnitude of the PL observed. It is posited that angles of 0° and 60° are critical to observe high intensity IX peaks, with suggestions that other twist angles may still produce PL but on a much smaller scale [65, 66]. Within our μm wide heterostructure shown in Fig. 5.2a), it is possible that there are lattice alignment changes, especially considering that each unit cell has a lattice constants of 3.15 Å and 3.28 Å for WS_2 and WSe_2, respectively, which may lead to spatially varying PL.

Additionally, after-effects originating from the monolayer transfer may also contribute to the inhomogeneity observed. During the stamping and cleaning process, portions of the monolayers may wrinkle and fold, particularly around edges, creating bilayer or even multilayer region in our TMDC. These surface irregularities increase the interlayer distance, which alters the IX emission intensity [67]. These physical effects likely explain the inhomogeneous response exhibited by IX_1 and IX_2 across the sample.

5.2.2 Temperature-Dependent Photoluminescence

Although the PL spectra taken at room temperature suggest that the peaks at ~840 nm and ~910 nm are interlayer excitons, further confirmation is needed. We can corroborate the findings using multiple methods including time-resolved photoluminescence, which enables us to measure the lifetimes such that IXs have longer (nanosecond-scale) lifetimes than the (picosecond-scale) intralayer exciton lifetimes [10]. This lifetime difference can be directly observed in the time-resolved spectra presented in Appendix A. Here, however, we focus on the temperature-dependent response of intralayer and interlayer excitons.

Fig. 5.3a) shows the PL measurements taken at 3 K of the WS_2/WSe_2 along with the bare monolayers. First, we consider the monolayers' spectra and the multiple excitonic peaks on display, which we attribute to various excitonic states such as neutral excitons, trions, and defect-bound excitons [68]. Moreover, we note that the WS_2 and WS_2 spectral peaks align with the first two peaks in the heterostructure PL. Interestingly, while the PL of the WS_2 exciton maintains the same relative intensity, the PL of the WSe_2 exciton decreases when going from bare monolayer to the heterostructure. This is a result of the formation of interlayer excitons in the WS_2/WSe_2 HS, which translates as holes remaining in the maximum of the valence bands, in the WSe_2 monolayer, and the electrons remaining in the minimum of the conduction bands, in the WS_2 monolayer. The quenching is a consequence of the interlayer formation rate being much faster than the intralayer recombination rate, such that electrons are more likely to transfer from WSe_2 to WS_2 than to recombine in the WSe_2 [69].

We attribute the final peaks appearing at around ~875 nm, which do not intersect with any monolayer emission, to the interlayer exciton. As shown in the full temperature-dependent PL (Fig. 5.3b), the intensity of the IX increases with decreasing temperature. This is partially caused by thermal energy, $k_B T$, decreasing as temperature decreases, such that there is insufficient energy for exciton dissociation. Hence, there are more excitons available to recombine and emit photons. Furthermore, the temperature decrease also results in a reduced phonon occupation which enhances the PL in two ways: 1) it decreases non-radiative recombination losses such that the intensity increases, and 2) it sharpens the spectral features [36]. This temperature-dependent sharpening of the WS_2, WSe_2, and the heterostructure PL features is more clearly displayed in Fig. 5.3c), 5.3d), and 5.3e), respectively.

At 3 K, the interlayer exciton demonstrates two highly distinguishable peaks at ~871 nm and ~884 nm along with other less resolved peaks, such as the ones at ~840 and ~855 nm. The appearance of multiple peaks likely corresponds to other interlayer emission peaks [69]. While the published peaks do not precisely match the wavelength observed in our results, likely due to differences in the samples, such as the substrate, hBN encapsulation, and strain [70, 64], the high number of peaks suggests efficient interlayer coupling in our HS. This could be due to a high fill factor (the number of excitons present per unit cell) that causes various cells to experience higher energies as a result of exciton-exciton repulsion [69].

Another proposition is that the two of the prevalent peaks correspond to the triplet (IX_T) and singlet (IX_S) exciton states. In particular, the peak at ~884 nm aligns with the emission previously determined to be the triplet interlayer exciton, IX_T [71]. Hence, the second peak at ~871 may coincide with the singlet interlayer exciton. IX_S. However, this assignment is challenged by an energy difference between the two peaks of approximately 20 meV, which is

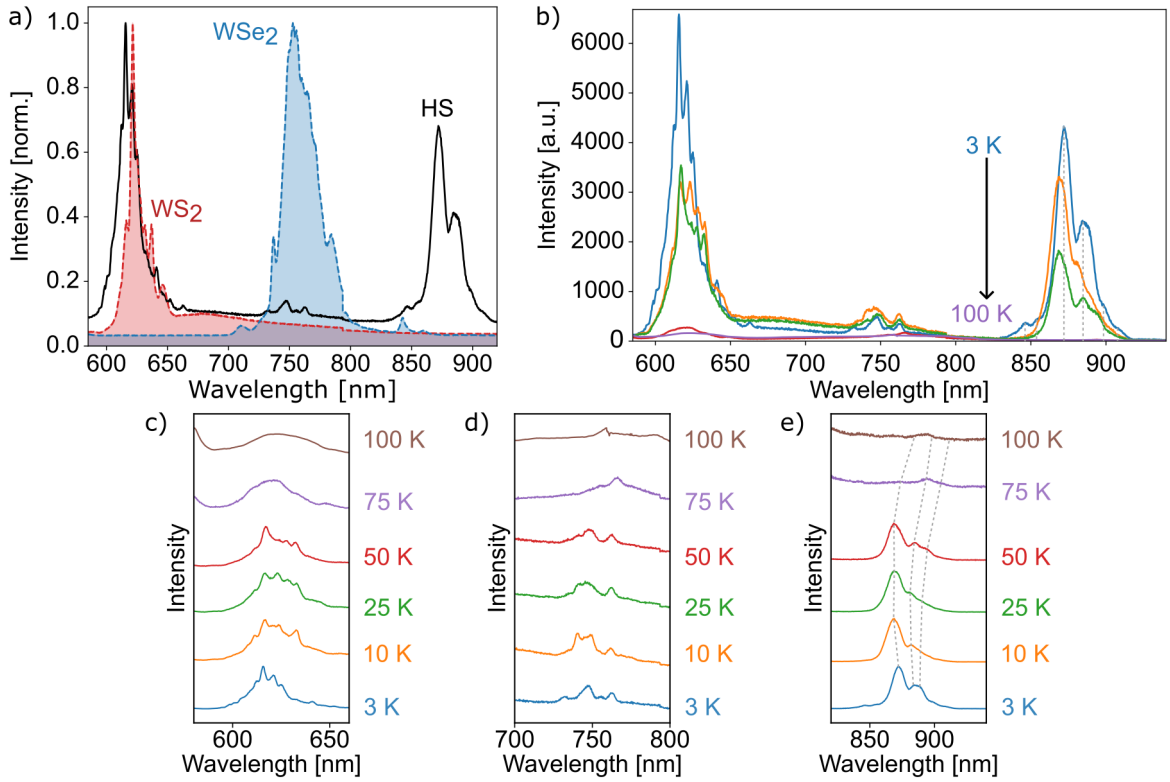

Figure 5.3: Plots displaying the temperature-dependent photoluminescence of a WS_2/WSe_2 heterostructure taken using a 504 nm laser with an incident power of ~1.28 μW. a) displays the whole spectra of the HS along with the spectra taken at WS_2 and WSe_2 individually, all taken at 3 K. b) shows the temperature-dependent PL from 3 to 100 K. c), d), e) display three individual sections in the PL spectra in order to observe the progression of the PL with temperature changes, offset for clarity. c) shows the spectra from 580 to 675 nm, d) shows the spectra from 700 to 800 nm, and e) shows the spectra from 800 to 950 nm. The colours of the lines and the temperature labels are consistent across all plots.

smaller than the expected spin-splitting of the WS_2 conduction band. Instead, the reported separation is more closely conserved when comparing the peaks at ~871 and ~855 nm, with an energy difference of 27 meV [71]. Hence, we establish the emission ranging from 840 to 920 nm to be the interlayer exciton with the individual peaks suggesting different excitonic behaviours, which enables deeper understanding of the exciton physics in this WS_2/WSe_2 HS.

Yet, considering that in 5.2.1 we observed two interlayer excitons labelled as IX_1 and IX_2, the temperature-dependent spectrum appears to display a single interlayer exciton from 850 to 920 nm. The reason for this discrepancy is not certain. However, observing the redshifting experienced during the transition from low to high temperatures, which is provoked by the band gap shrinking due to the expansion of the lattice [19], we expect the IX_2 exciton to reside below ~840 nm. The grey dotted lines corroborate (Fig. 5.3e) this, as they indicate the peak shifts from shorter to longer wavelengths with higher temperatures. This suggests that the emission we observe at 850-920 nm belongs to IX_1. However, it is essential to note that accurately resolving the peaks at 75 and 100 K is challenging, such that the grey lines at higher temperatures only function as guides for the eye. Thus, the low-temperature interlayer exciton emission most likely evolves into the IX_2 peak ($\lambda = 910$ nm) observed at room temperature.

5.2.3 Power-Dependent Photoluminescence

To further confirm the type of exciton observed, we measure laser-power-dependent photoluminescence of excitons. The excitons follow a power law:

$$I_{PL} = P^{\alpha}, \tag{5.1}$$

where I_{PL} is the PL intensity, P is the incident power, and α is the exponent that helps identify the nature of the exciton. The expectation is that, by changing the laser power, we will observe different rates of intensity increase depending on the type of exciton.

To measure the power dependence, we use the method described in 3.2.3 to probe the HS at 3 K using laser powers ranging from 0.39 μW to 100.70 μW. The incident power is measured before it enters the cryogenic chamber with a ThorLabs PM16-122 power meter, ensuring that we record the incident power as accurately as possible. The resulting spectra, from which we obtain the total intensity per laser power by integrating under each emission peak, are shown in Fig. 5.4a).

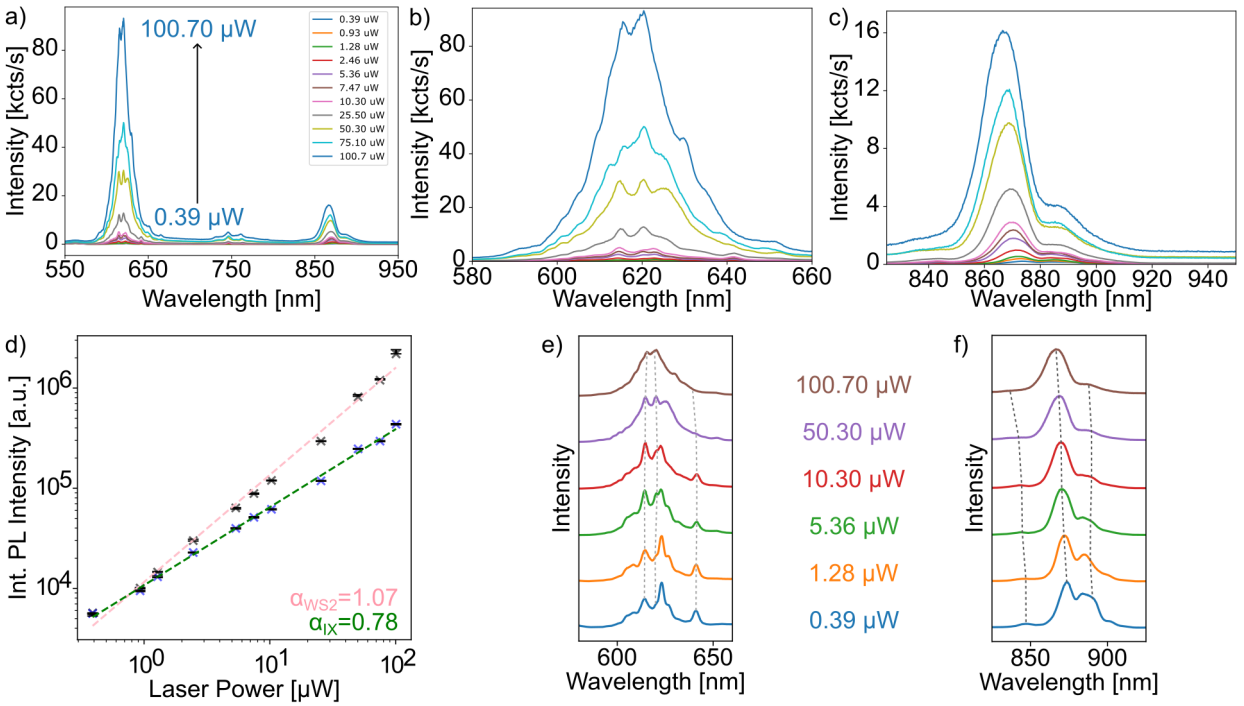

Figure 5.4: Plots showing the laser-power-dependent PL spectra of our WS_2/WSe_2 HS. a) displays the full spectra with b) giving a closer look at the PL between the ranges of 580 and 660 nm where the WS_2 intralayer excitons reside. c) is a closer look at the peak in from 820 to 950 nm, which, given the range, we intuit to be an interlayer exciton. PL intensities in a)–c) are given in kilo-counts per second (kcts/s), normalized to integration time. d) is a logarithmic plot of integrated intensity as a function of power with the corresponding points for each power and two fitted lines with an α of 1.07 and 0.78, for the WS_2 intralayer exciton and the interlayer exciton, respectively. e) and f) show the spectral dispersion of the two distinct peaks as a function of laser power.

To confirm the accuracy of the power measurements, we use the higher resolution WS_2 intralayer exciton emission as the reference to which we compare our interlayer exciton. Examining Fig. 5.4, both the WS_2 and IX emissions show substantial growth, but, at the highest power, the WS_2 emission (Fig. 5.4b) reaches ~80,000 counts while the IX emission only reaches ~16,000 counts (Fig. 5.4c). The data obtained after integration under their respective photoluminescence spectra is displayed in Fig. 5.4d), with the pink line indicating the WS_2 exciton integrated intensity, the green line indicating the IX integrated intensity, and the gradient of both revealing their α values. For intralayer excitons, typically, near-linear or linear values such as α = 1.0 for WSe_2 [72] are reported. In contrast, the expected α for IX is sublinear, with values as low as α = 0.3 being reported for a TMDC heterostructure [21]. The difference in the power-dependent rate of growth and thus the linearity of α is a result of the higher exciton-exciton annihilation, dipolar repulsion and state-filling experienced by the interlayer exciton [21].

Comparing this with the experimental results extracted from Fig. 5.4d), we obtain a near-linear $\alpha_{WS_2} = 1.07$ close to the value expected for intralayer excitons as well as an expected sublinear α_{IX} with a value of 0.78. Both values coincide with the reported power-dependent trend for their respective exciton, however, while our experimental α_{IX} is

sublinear it does have a comparatively larger value than the example. The offset between the reported α and the fitted α_{IX} likely arises from differences in the dipole-dipole repulsion experienced by the heterostructure [21]. Hence, the power-dependent measurements for both the WS_2 and interlayer excitons agree with literature, which further proves that the emission from 840-920 nm is indicative of our WS_2/WSe_2 interlayer exciton.

The spectral dispersion of these emissions, and their features, are displayed in Fig. 5.4e) and f), with the grey dotted lines acting as guides. The evolution of the peaks shows the expected blue shift with increasing power, with literature showing power-dependent PL measurements utilising powers as large as 3.4 mW producing an even larger blue shift [22]. This is due to conduction band-filling which induces dipole-dipole repulsion [71] and widens the band gap. However, even though higher incident powers blue-shift and enhance the overall emission measured, the individual features observed in the WS_2 and IX emissions scale at different rates with increasing power.

Closer examination of the peaks demonstrate that some remain distinct at all incident powers while others diminish with increasing power. This effect is noticeable when observing the interlayer exciton features in Fig. 5.4f), and is further evaluated by fitting the peaks with a sum of Lorentzians function. At low excitation power, Lorentzian fitting identifies three peak centers at ~882 nm, ~875 nm, and ~870 nm, with corresponding α values of 0.53, 0.80, and 1.12, respectively. While, 0.53 agrees with literature that indicates the presence of a triplet IX at ~882 nm, the other values deviate from the expected singlet IX exponent of 1.04 [20]. Based on these results, we infer that one emissive peak does experience greater radiative efficiency compared to the other as noted by the respective superlinearity and sublinearity. Moreover, previously, we suggested that the two significant peaks can be described as the singlet IX and triplet IX. This is corroborated by the faster growth in IX_S (1.04) than in IX_T (0.54) with increasing power [20], since, at higher excitation powers, electrons are more likely to occupy higher-energy states that favour IX_S formation [71]. As such, this power-dependent measurement allow us to both confirm the presence of an IX and also examine the nature of some of the individual IX peaks that emerge at low-temperature regimes.

5.3 Reflectivity

The final optical characterisation performed is reflectivity, aimed at gaining insight into how the WS_2/WSe_2 heterostructure absorbs incoming photons. These measurements were taken in the cryostat setup illustrated in Fig. 3.3, with a halogen lamp (OSL2 Fiber Illuminator) that replaces the laser source to probe a wider spectral range across an array of temperatures.

As shown in Fig. 5.5a), the reflectance increases at the excitonic wavelength, which is most pronounced at low temperatures. This is largely caused by a reduction in phonons at low temperatures, which leads to a decrease in non-radiative recombination. The phonon reduction itself is a product of lower thermal excitation [36], which altogether leads to improved quantum yield and the appearance of distinct excitonic reflectance peaks. Figure 5.5a) displays the raw reflectivity data for each component of our sample: the WS_2 1L, the WSe_2 1L, their intersection (the HS), and the SiO_2 substrate used as the reference. We subtract the dark counts from these spectra to ensure more accurate absolute reflectance values. The processed data (Fig. 5.5b) shows that all components, with exception of the SiO_2 substrate, possess prominent peaks that align with excitonic states. For the WS_2 and WSe_2 reflectance spectra, the peaks coincide with the expected location of A-excitons at 10 K of ~610 nm and ~720 nm, respectively [19].

These same two peaks displayed in the HS reflectance spectrum, with the exception of some slight deviations. Particularly, the peaks at ~610 nm and ~720 nm are slightly broader and red shifted in the HS spectra. We hypothesize that these differences are linked to the interlayer coupling and possible strain on the interface [69].

More interestingly for the HS, no other peaks appear around the range where the IX photoluminescence appeared. This is reasonable as reflectivity probes direct optical transition, meanwhile PL relays additional information on any indirect or multi-step processes occurring, such as multi-step IX formation. Thus, the absence of peaks at wavelengths above 800 nm suggests that the direct IX excitation exhibits a weak oscillator strength. Instead, we suggest a two-step IX formation mechanism: 1) the electron promotion within the monolayer, followed by 2) the transfer from the original conduction band to the next. The absence of a peak at IX wavelength for all temperatures from 3 to 100 K

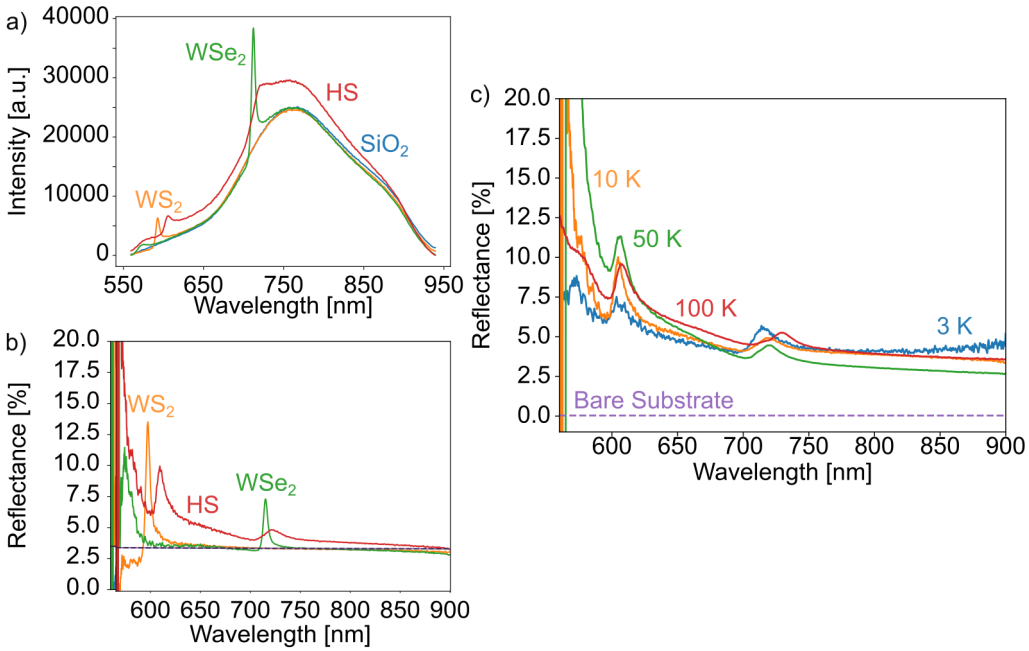

Figure 5.5: Reflectance of our WS_2/WSe_2 HS at a) 10 K taken for both the individual materials, the HS, and the SiO_2 substrate (raw data). b) shows the absolute reflectance calculated from a) with the dotted line marking the theoretical and experimental reflectance of SiO_2. c) displays the absolute reflectivities at 3, 10, 50, and 100 K.

(Fig. 5.5c) further reinforces the likelihood of a multi-step IX formation mechanisms in the HS. Here, the existing peaks in the temperature-dependent reflectivity demonstrate a gradual red-shift provoked by increasing temperature, as discussed in 5.2.2. Furthermore, the HS also demonstrates an overall increase in reflectance as a consequence of the high refractive index of bilayer regions [73]. As a result, it is likely that direct optical transitions in the WS_2/WSe_2 configuration are primarily dictated by the WS_2 and WSe_2 A-excitons.

With this reflectance data, along with the previous optical measurements, we demonstrate the clear physical and electronic coupling achieved using large-area stamping. Furthermore, we obtain a greater understanding of the HS and its underlying optical mechanism, particularly the multi-step IX formation and emission, which we can now employ in the fabrication of our WSe_2/WS_2 device.

Chapter 6

Fabrication of a 2D Heterobilayer Device

In this chapter, we design, fabricate, and test a heterobilayer device for PV applications. We begin by explaining how the device was designed for maximum solar spectrum absorption (6.1). This is followed by confirming the successful fabrication using the optical characterisation methods of Raman spectroscopy, photoluminescence, and reflectivity (6.3). Finally, we investigate the device's electrical response through IV measurements (6.4) under LED illumination and EQE measurements (6.5), which probe the wavelength-dependent photoresponse.

6.1 Enhancing Optical Absorption through hBN Thickness Tuning

In a multilayer thin-film stack, the reflection and transmission at the interfaces are described by the Fresnel equations. The numerous internal reflections within the stack lead to the calculation of total transmittance and reflectance becoming algebraically complex. The transfer matrix model (TMM) simplifies this process by using a matrix formalism that takes the incident field magnitude as input and outputs the net reflectance and transmittance through the summation of forward- and backwards-propagating vectors. This facilitates the calculation of reflectance and transmittance for any thin-film stack, provided that the refractive indices of each layer are known.

While the TMM directly outputs transmittance and reflectance, we are more concerned with maximising the absorbance, a critical metric for PV devices. We use the energy conservation relation to extract the absorbance (A) from the TMM calculated transmittance and reflectance, such that:

$$A = 1 - (T_{\text{total}} + R_{\text{total}}), \tag{6.1}$$

where T_{total} and R_{total} denote the total transmittance and reflectance, respectively.

In this thesis, we use Steven Byrnes' TMM package [74] to reproduce published results and optimise the hBN thicknesses, which will be incorporated into the final WSe_2/WS heterobilayer device. The photovoltaic device we envision is intended to maximise the absorption of the solar spectrum by enclosing the HS between two hBN flakes of varying thicknesses and a gold contact acting as a back reflector, as shown in Fig. 6.1a) and b). Here, the gold contact aids in increasing the absorption by forcing unabsorbed light to pass through the absorber layers a second time [75]. Meanwhile, the optical properties and the lack of dangling bonds of hBN make it an attractive insulator [76]. Our objective is to identify the optimal hBN combination that achieves the highest solar spectrum absorption.

The initial computation is the integrated absorption across the 397–825 nm range for combinations of hBN thicknesses ranging from 0 to 150 nm (top) and 0 to 160 nm (bottom). However, this computation fails to account for fluctuations in the solar spectrum, as it gives all wavelengths equal importance. Thus, to find the weighted absorption spectrum, we integrate the product of the normalised solar photon flux (Fig. 6.1b), $\phi_{\text{p}}(\lambda)$, with our original absorption spectrum, $Abs(\lambda)$:

$$A = \int_{\lambda_i}^{\lambda_f} Abs(\lambda) \cdot \phi_{\text{p}}(\lambda)\, d\lambda \tag{6.2}$$

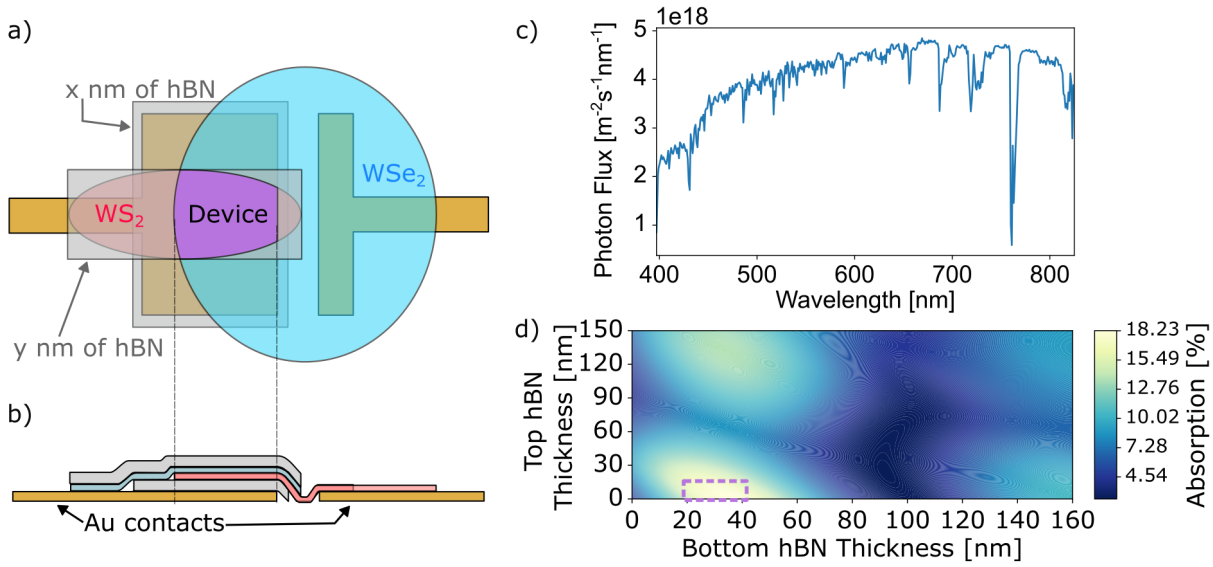

Figure 6.1: Schematic of the a) top view and b) the side view of the initial device design for input in the transfer matrix model (TMM). The hBN flakes are labelled as x and y nm thicknesses to indicate that these are the variables we are optimising. c) Plot showing the solar photon flux with respect to wavelength from 397 to 825 nm calculated from the AM15G spectral irradiance [77]. d) Colour map showing the integrated absorption weighted and normalised by the photon flux shown in c). The strength of the absorption is indicated by the brightness of the map, with lighter colours indicating higher absorption. The purple box marks the hBN dimensions that theoretically result in the highest weighted absorption.

where $\lambda_i = 397$ nm and $\lambda_f = 825$ nm. The output is further refined by normalising the weighted absorption by the maximum solar photon flux value to display solar absorption as a percentage.

We find that, according to the simulation (Fig. 6.1c), the optimal absorption occurs when we have a bottom hBN thickness of 35 nm and no top hBN layer, with a 18.23% absorption of the solar spectrum. The lack of top hBN could be a result of the reflectivity increasing significantly, while a 35-nm-thick hBN flake optimises the vertical position of the WSe_2/WS_2 HS by aligning it with the electric field maximum to enhance the light-matter interaction.

The relatively low absorption of 18.23% may be attributed to several causes. First, the expected absorption losses may partially be a consequence of reduced absorption occurring at wavelengths longer than the band gaps of WS_2 and WSe_2 and their resulting HS, with the limit residing at ~910 nm (IX_1 peak). More importantly, the TMM does not account for interlayer excitons in an HS. This is attributed to the limited input variables [74] rather than the model itself: the complex refractive indices used are calculated from each material's refractive index (n) and extinction coefficient (κ), so they are unable to capture any IX effects. Additionally, the reduced absorption may stem from the longitudinal propagation of light through the HS, which limits the interaction strength within the atomically thin layers. As such, while the TMM provides a good approximation of the absorption in the device stack, we expect the experimental results to deviate from the calculations due to missing excitonic effects.

6.2 Three-Step Stack Fabrication of the Device

With the material selection, layer thickness, and the stacking order optimised for absorption, we proceed to fabricate the HS device illustrated in Fig. 6.2a). This is performed in three steps consisting of transferring 1) the hBN onto the Au contact, 2) the WSe_2 monolayer on top of the hBN, and 3) the WS_2 monolayer on top of everything

To obtain the desired 35-nm-thick hBN flake, we exfoliate hBN crystals (obtained commercially from 2D semiconductor), using the Scotch tape exfoliation method [5] until we obtain a range of thinner flakes. We transfer the freshly cleaved hBN flakes onto TRT, which we paste onto SiO_2 substrates. Then, we remove the TRT by heating the substrate, using a hotplate (IKA RCT Basic), to 110 °C. This is followed by a longer 30-minute heat treatment to remove

any adhesive residue.

The hBN transfer is adapted from the monolayer transfer protocol (4.2) to account for the difference in surface energies between TMDCs and hBN. Prior to stamping, the LDPE and the superglue drop are treated with 2 minutes of air plasma to increase the adhesion between them as the air plasma increases the compatibility of the materials by physically altering their surface energies [78] and increases the likelihood of hBN pickup.

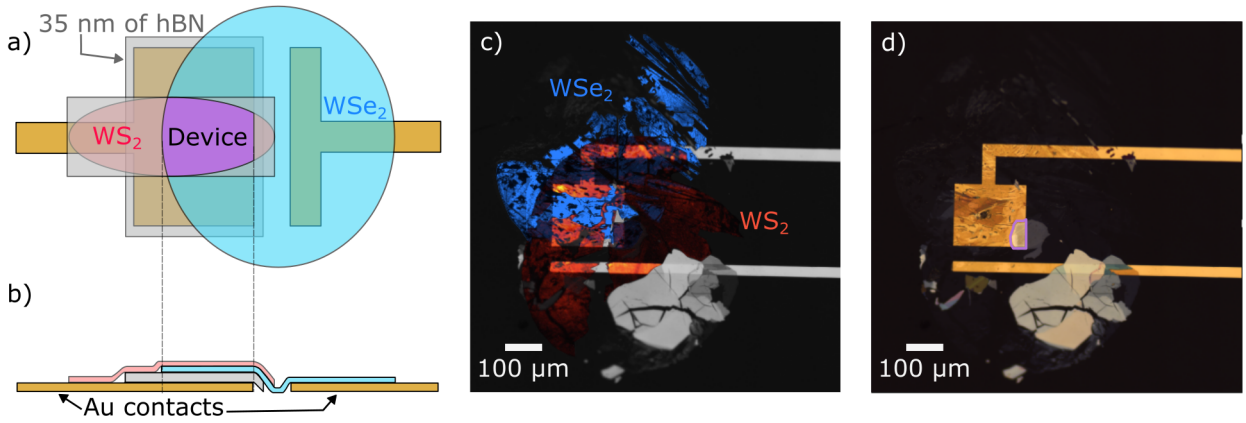

Figure 6.2: Illustration of the structure and stacking order of the solar absorption maximised PV device with a bottom hBN flake of 35 nm from the a) top and b) side. The purple area indicates the only area where all the needed components are stacked on top of each other, indicating the device. The grey dotted line acts as a guide to demonstrate the equivalent overlap in the side view. c) and d) show the actual device, but c) uses wide-field photoluminescence images of each monolayer on top of each other to provide a better visual understanding of where each layer lies.

The following step involves picking up the 35-nm-thick hBN flake, which is found by matching the experimental reflectivity with the theoretical reflectivity generated by an hBN flake of the same thickness. We align the superglue drop minima with the hBN flake and use a motorised stage to perform a controlled descent of the stamp (at a speed of 2 mm/s and an acceleration of 2 mm/s^2) at 70°C until the entire hBN flake contacts the LDPE. The LDPE is quickly separated from the substrate at the same speed and acceleration, which results in the hBN flake lying on top of the stamp. The transfer onto the Au contacts lying on a SiO_2 substrate follows the same protocol as described in (4.2) . After finalising the drop, we ensure the removal of the solidified LDPE by using two cleaning techniques: OA cleaning at 130°C for 30 minutes, followed by 5 minutes of plasma cleaning with air. The air plasma treatment also aids in removing residual OA and organic contaminants remaining on the hBN and gold.

After the hBN is transferred onto the gold contact, the next step is to perform a WSe_2 transfer onto the hBN flake, while verifying that the monolayer contacts only one of the two contacts (Fig. 6.2b). This placement is crucial for creating a proper heterojunction, which enables charge separation and directed diffusion towards their respective contacts.

Finally, we complete the stack by transferring WS_2 with the intention to stamp it onto the opposite electrode to complete the junction. The final prototype is shown in Fig. 6.2d). However, Fig. 6.2c) shows that WS_2 is stamped across both contacts, resulting in the device lacking a well-defined junction. Consequently, this may alter the expected asymmetric photovoltaic photocurrent response into a more symmetric response, as electrons may bypass the heterointerface.

6.3 Optical Spectroscopy

6.3.1 Raman Spectroscopy: Probing Physical Coupling

After fabrication, we characterise the device's Raman response to confirm whether our two monolayers are in contact with each other. Fig. 6.3a) shows the mapped area, which encompasses the Au/hBN/WSe_2/WS_2 stack.

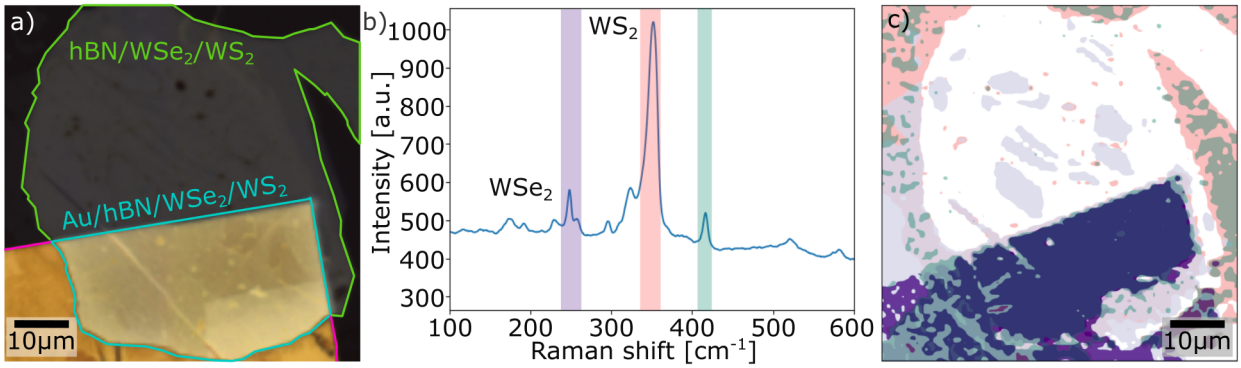

Figure 6.3: a) The bright-field image corresponding to the area being mapped using Raman and, later in 6.3.2, using PL. The border corresponds with the different material configurations, with the device being bordered in blue. The hBN/WSe_2/WS_2 is bordered in green, the Au/WSe_2/WS_2 is in pink, and the remaining area is just WSe_2/WS_2 on SiO_2. b) Raman spectra taken at a spot with all the layers (Au/hBN/WSe_2/WS_2) in the device. The peak at 250 cm^{-1} corresponds to WSe_2, the peaks at 350 and 415 cm^{-1} correspond to WS_2. The enhancement of the peak at 415 cm^{-1} indicates the presence of a WSe_2/WS_2 heterostructure. c) The resulting layered map of the integrated Raman peaks observed in b) with the highlight colours corresponding to the peaks. Only the highest-intensity areas for each peak are shown on the map, with the main overlap occurring at the edge of the gold contact (highlighted in blue). The white section indicates the location of the hBN flake outside the gold contact.

The measured spectrum (Fig. 6.3b) shows all the expected peaks for WS_2, WSe_2, and the heterostructure. However, the Raman map displays a large "white space" that aligns with the shape of the hBN flake highlighted in green in Fig6.3a), which suggests that there are no vibrational modes and thereby no monolayers present. However, the lack of colour does not prove the lack of monolayers. As shown in Fig. 6.2b), hundreds of μm sized monolayers are clearly stamped across the electrodes. The apparent lack of Raman signal is due to intensity damping, which is influenced by the twist angle.

Specifically, the A_{1g} (250 cm^{-1}) mode of WSe_2 experiences damping at angles approaching 0° and 60° as a result of the interlayer coupling, which causes a change in polarizability of the (out-of-plane) vibrational mode [35]. This is also reflected in the low intensity A_{1g} peak shown in Fig. 6.3b), while the in-plane WS_2 E_{2g} (350 cm^{-1}) mode is enhanced at small twist angles. Additionally, the peak highlighted in green belongs to the WS_2 A_{1g} (415 cm^{-1}) mode, which is typically significantly enhanced by the presence of interlayer coupling [35] . These collective changes in Raman intensity confirm contact and suggest some degree of physical interlayer coupling between the TMDC monolayers in the device.

6.3.2 Photoluminescence spectroscopy: Probing Electronic Coupling

While Raman spectroscopy provides clear insight into the physical coupling of our WSe_2/WS_2 heterostructure, we confirm the electronic coupling using PL spectroscopy. As noted in 5.2.1, the presence of IXs at room temperature is indicative of strong interlayer coupling between layers.

Figure 6.4a) shows the spatial maps for the WS_2 and WSe_2 A-exciton, as well as IX_1 and IX_2. However, we also display a second map (Fig. 6.4b) with no IX_2, as the PL spectrum shown in Fig. 6.4c) demonstrates the difficulty in

resolving the IX_2. The lack of resolution may concern a large reduction in intensity such that IX_2 is completely hidden in the shoulder of the IX_1 emission. Nonetheless, regardless of the uncertainty of IX_2, we can still resolve three peaks consistent with the typical WS_2 (~620 nm), WSe_2 (~740 nm), and, critically for the electronic coupling of the layer, IX_2 (~840 nm) emissions (Fig. 6.4b).

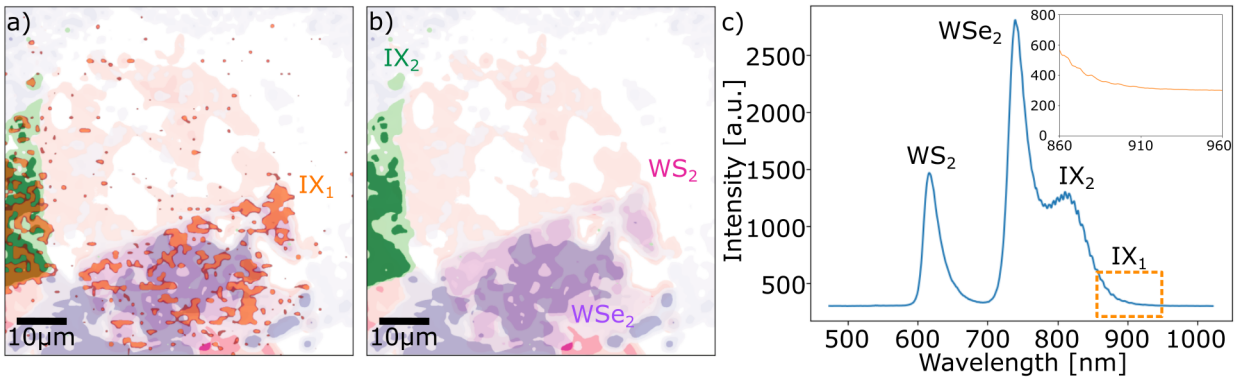

Figure 6.4: a) The layered PL map with each layer being the integrated intensity under each exciton peak in c), with an additional fourth layer representing the PL at 910 nm. b) shows a PL map without the intensity corresponding to IX_1 (orange). WSe_2, WS_2, and IX_2 are coloured pink, purple, and green, respectively. c) Photoluminescence spectrum taken at a point where, according to a), both interlayer excitons, IX_1 and IX_2, are present. The orange box marks the spectrum taken as an inset. The inset closely shows the PL at 910 nm, where IX_1 is usually shown.

Unexpectedly, the IX_2 signal appears strongest just outside the edge of the Au contact and the hBN flake, where we probe the WSe_2/WS_2 lying on top of the SiO_2 substrate. Although Raman spectroscopy confirms the presence of the HS on the Au/hBN region, we hypothesise that loss of IX_2 may be attributed to a low Purcell factor (suppression of spontaneous emissions [79]) and a small field overlap at the heterointerface. It may also be a result of differences in local strain, defect-states, or exciton-phonon interactions [80, 81], which affects the non-radiative recombination and linewidth.

6.3.3 Reflectivity: Insight into Absorption Mechanisms

To complement the PL spectroscopy measurements, we use reflectivion spectroscopy to explore the excitation mechanism in the device.

Figure 6.5 reveals two distinct dips corresponding to the WS_2 and WSe_2 intralayer A-excitons, which align well in wavelength with the peaks predicted by the TMM. However, while the WS_2 exciton peaks closely match the calculated spectrum in depth and position, the WSe_2 exciton dip appears more than 20% lower than predicted. This discrepancy may suggest that the WSe_2 exciton induces higher absorption than expected.

In contrast, we observe no clear dips associated with IXs. This supports the hypothesis that direct optical excitation of IXs is unlikely (5.3). Instead, we propose that IX formation is an indirect, multi-step process involving the charge transfer between conduction bands. However, it is important to note that the artefacts introduced by the narrow bandwidth of the LED source (when $\lambda \geqslant$ ~900 nm) limit the visibility of dips in these regions. Therefore, while the reflectivity data confirm the direct intralayer excitation, they do not rule out the possibility of direct interlayer excitation, particularly for IX_2.

More broadly, when comparing the experimental and theoretical reflectivities, we note that the theoretical reflectivity reaches values above 80% while the experimental reflectivities peak at around 60%. As mentioned, this overall reduction may indicate an ideal enhancement in absorption. Oppositely, it may also be a result of the different refractive index sources used to calculate the material reflectivity, or neglected scattering losses [15].

Comparatively, the reflectivity of the device is enhanced to the isolated HS (Fig. 5.5b). This enhancement is likely

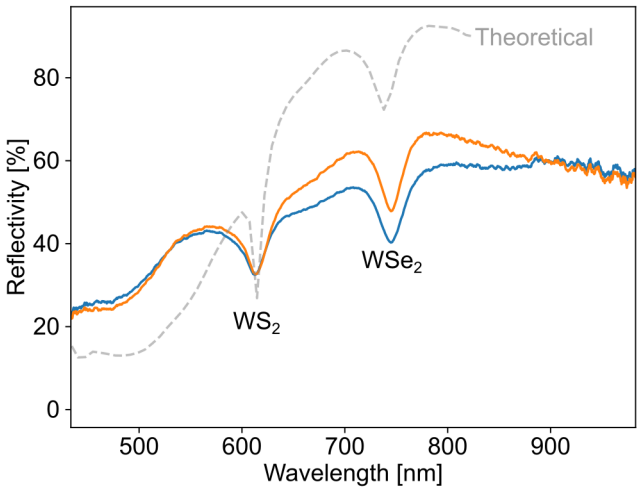

Figure 6.5: Reflectivity of the device measured using the SiO_2 substrate as the reference compared to the theoretical reflectance (grey) calculated using TMM. Both measurements exhibit dips at 620 nm and 740 nm, which align with the WS_2 and WSe_2 excitons. An additional dip is seen at ~520 nm as a result of the WS_2 B-exciton.

due to the optical cavity formed by the hBN flake and the underlying gold contact, which acts as a back reflector. This increases the quantity of light constructively interfering, which increases the reflectivity across the spectrum (and particularly off-resonance). This contrasts with the HS fabricated on transparent SiO_2 measured in Fig. 5.5b), which lacks an optically coupled back-reflector. Thus, we experimentally demonstrate that the device's design successfully increases the likelihood of absorbing incoming light.

Overall, the reflectivity measurements provide insight into wavelength-dependent absorption and, therefore, the excitation pathways in the device. However, further characterisation, particularly electrical, is needed to obtain a more comprehensive understanding of the role of intralayer and interlayer excitons in the device photogeneration.

6.4 Current-Voltage Characterisation

6.4.1 Dark Current

Before testing the device under illumination, it is crucial to measure the dark current (the current flowing through the device without incident light) to evaluate its intrinsic electrical properties. The IV curve in Fig. 6.6a) shows its low current response (on the order of tens of picoamperes) across a voltage sweep from -10 V to +10 V. The individual measurements exhibit significant fluctuations due to a low signal-to-noise ratio, which reduces their accuracy. Therefore, we measure the IV response five times in between 30 seconds of rest to obtain the average response with the error corresponding to one standard deviation (light blue), as shown in Fig. 6.6b).

The first observation is the presence of a hysteresis, which is the difference in response between the forward and reverse voltage sweeps. In monocrystalline TMDCs, the cause of this hysteresis is mainly charge trapping at defect sites and atmospheric molecules (e.g. O_2 and H_2O), which retain and release carriers at later points in the sweep [82]. The extent of this hysteresis can be exacerbated by the sweep rate, such that slower sweeps result in higher charge trapping in the TMDC and at their interface [82].

Another source of hysteresis is the Schottky barrier at the metal-semiconductor interface. In our device, the barrier is formed at the Au-TMDC interface due to differences in work functions, resulting in an increase in the minimum energy required for carrier transfer from the semiconductor to the metal. This Schottky barrier height amplifies the charge trapping, thus further enhancing the hysteresis [7].

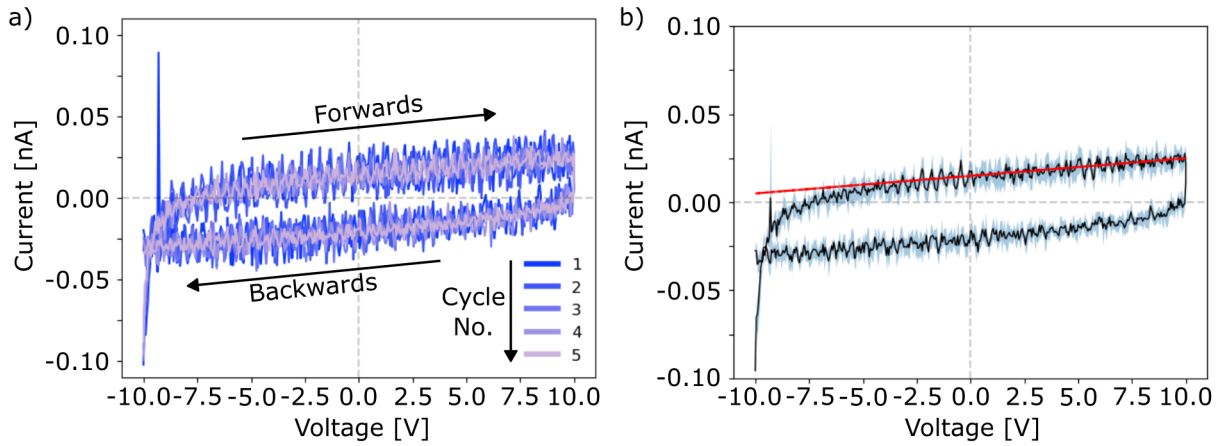

Figure 6.6: IV measurements taken under dark conditions to see the intrinsic electric properties of our device. a) shows the current response for voltages doing sweeps from -10 to 10 V for consecutive cycles, with each increasing cycle being plotted in a lighter colour. b) refers to the average dark IV current response, with the blue outline indicating the standard deviation and the red line acting as the line of best fit for the forward response.

Regardless of the hysteresis, both the forward and backwards sweeps appear to display a linear relationship, as shown by the fit made using Ohm's law to extract the series resistance (Fig. 6.6b). The resulting line resembles that of an ohmic device (Fig. 3.4b). However, this is undesirable for a PV device, which should exhibit rectification (i.e., a desired direction of carrier flow). Instead, we observe the absence of threshold voltage and rectification, as noted by the symmetric response [7] . This observation is corroborated by Fig. 6.2, where, instead of placing each monolayer on its respective contacts, WS_2 overlaps both. The overlap eliminates the possibility of possessing a well-defined heterojunction through which IX formation, dissociation, and charge separation can occur. This suggests that a certain percentage of carriers drift solely across the top WS_2 monolayer rather than through the WS_2/WSe_2 interface.

Charge separation and electron drift are further hindered by high resistance. The resistance, R, of a device is the inverse of the slope of the curve such that:

$$R = \frac{V}{I}, \tag{6.3}$$

where V is the applied voltage and I is the measured current. Using the linear fit shown in Fig. 6.6b), resistance is calculated as an extremely high ~100 GΩ. This high resistance is attributed to two types: series and sheet resistance in monolayer [83].

Series resistance originates from the inherent material resistances of the semiconductors, the metal contacts, and the contact resistance (the resistance felt at their interface). While the Schottky barrier once again plays a pivotal role, the series resistance is also affected by interface defects, contamination, Fermi-level pinning, and surface area [84]. Moreover, sheet resistance is a particularly critical in thin films such as TMDCs. It describes the in-plane transport behaviour of carriers in 2D materials, and, due to the thinness of atomically-thin materials such as monolayers, they can be partially categorised as an intrinsic property of these materials [85]. The sum of these two factors significantly limits the intrinsic charge transport.

6.4.2 Photocurrent Response Under LED Illumination

While we understand the current response in the dark, the most important test for a PV device is its response under illumination. We use a super-bright white-light LED to simulate the visible range of broad-spectrum solar illumination. The resulting IV measurements are shown in Fig. 6.7a).

Compared to dark conditions, incident illumination results in a significant increase in current (by a factor of 10),

particularly under forward bias. The changing R shows that the device possesses variable resistance. This demonstrates the photoconductive nature of TMDCs, which are influenced by incident light.

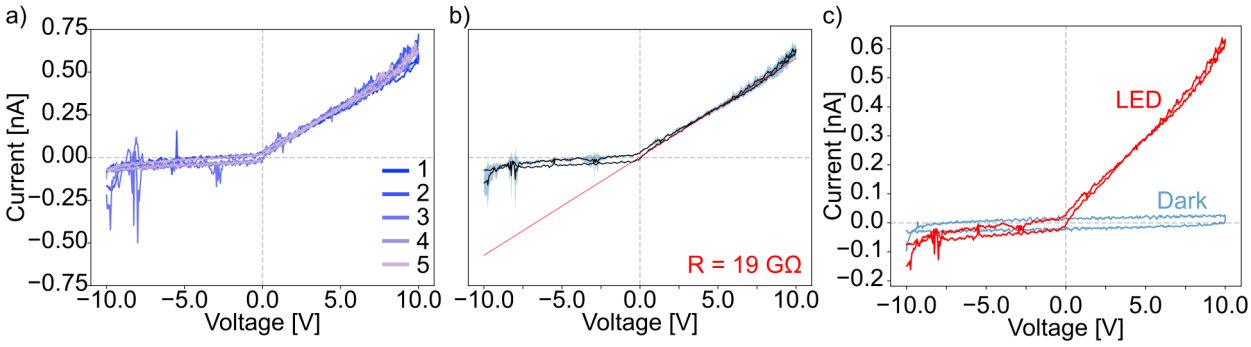

Figure 6.7: Current response to voltages sweeping from -10 to 10 V under illumination. a) and b) are the responses under 100% LED illumination, with b) being the average of the consecutive cycles shown in a). The red lines mark the best fit according to the data. c) superposes the dark and LED current measurements to compare the effect of illumination on the current response of our device.

In a photoactive device, the increase in current with incident light occurs because the carrier density increases. This density increase is a result of a larger number of electrons excited by photons with energy greater than the bandgap [7]. Consequently, the resistance decreases by a factor of 50 from ~100 GΩ (in the dark) to ~19 GΩ (under illumination), shown in Fig. 6.7b).

Comparing the IV curves in the dark and under illumination in Fig. 6.7c), we conclude that photoexcitation and carrier generation play a pivotal role in the current enhancement. Additionally, we observe an asymmetric response under illumination, suggesting some contact or path asymmetry such that charge carriers exhibit a preferred transport direct. However, despite this asymmetry, the IV response retains it ohmic nature, indicating the absence of rectification. This further corroborates the absence of a well-defined heterojunction for charge separation, suggesting that when probing the wavelength-dependent EQE, we may not observe absorption at IX resonances.

6.5 Visible Spectrum External Quantum Yield

Fig. 6.8 shows the EQE in the visible spectrum from 460 to 670 nm. Across this range, our device demonstrates a measurable electrical response on the order of 10^{-6}. Notably, it exhibits stronger EQE peaks at ~620 nm and ~520 nm, corresponding to the A- and B-excitons of WS_2, respectively. This suggests that the intralayer exciton is a crucial feature in the photoelectric effect within the heterostructure device.

Accordingly, the expectation when measuring at wavelengths longer than 670 nm is to observe EQE peaks corresponding to the WSe_2 A-exciton (~740 nm), and potentially, IX peaks beyond that wavelength. The intensity of IX peaks may be dampened due to a multi-step IX generation process (6.3.3), which favours the creation of intralayer excitons that are later converted into IX. However, our attempt to measure EQE in the near-infrared and infrared ranges (690–950 nm) resulted in noisy data with no indication of an excitonic peak.

Their absence may be explained by several hypotheses ranging from the measurement equipment to the device itself. First, we note that the NKT laser produces a lower power output in the near-infrared and infrared ranges, which reduces the number of incident photons and thus the number of electrons collected. Second, EQE measurements at longer wavelengths may exhibit reduced absorption in a TMDC HS device due to the limited thickness of the 2D materials. Furthermore, charge carriers produced using longer wavelengths may have insufficient energy to overcome potential barriers corresponding to resistance, limiting electron collection. Finally, the reduced signal may simply reflect that the WSe_2 is not properly electrically contacted, which is corroborated by the strong reduction in EQE at wavelengths larger than 650 nm (Fig. 6.8). In general, the low signal at long wavelengths is likely attributed to a combination of all these factors, which can be addressed by improving upon this first device.

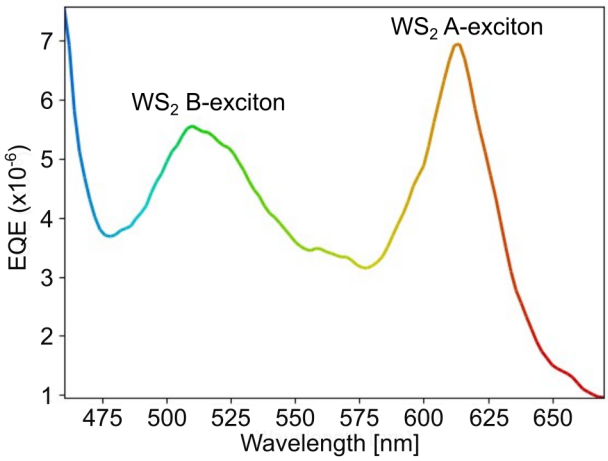

Figure 6.8: EQE measurement taken on the heterobilayer device at visible wavelengths using the NKT SuperK Select. The colour of the line in this plot matches the colour of the laser at each respective wavelength. The EQE at near-infrared and infrared wavelengths could not be measured due to the high signal-to-noise ratio.

6.6 Limitations and Improvements to the Current Device

First, the IV measurements with a non-zero start and end voltage produce some imprecision in the results due to a sudden voltage spike. The immediate improvement should involve modifying the code that controls the voltage sweeps so that, regardless of the maximum and minimum voltages, the sweep begins at zero. The modification protects the device from sudden voltage-induced damage, but also removes the imprecision observed at the beginning of the sweep (Fig. 6.7a).

Otherwise, we also take note of the weak EQE response of our device (on the order of 10^{-6}) seen in Fig. 6.8 and unmeasurable response in the NIR/IR range. This is partly caused by the high resistance, which is achieved through the combination of contact, sheet, and series resistances that collectively create very high resistances. This is also demonstrated when looking at the IV result, particularly the low photocurrent response even at 10 V. Increasing the photogenerated response and reducing the resistance requires better materials for contacts, such that their work function pairs better with WS_2 and WSe_2.

The strength of the signal may also be improved by increasing the thickness of the monolayers. While TMDC monolayers have a high absorption coefficient (Fig. 6.1a), they are also atomically thin, causing them to only absorb a small portion of incoming light even if optimised. For this reason, if the intention is to fabricate a 2D PV with the optimal power and efficiency, the design should utilise thicker multilayer TMDCs in the heterostructure to ensure that the increasing material thickness causes a respective increase in light absorption.

Finally, the absence of a WSe_2 exciton in the EQE may be caused by it not being properly electrically contacted. This issue may be addressed by fabricating a new 2D HS device that achieves a well-defined junction, thereby making IX generation more effective. Conversely, the current device may also be annealed to reduce strain, interfacial bubbles, and contamination, and improve interlayer coupling [86]. Annealing may result in the proper electrical contact between the Au contact and WS_2.

Ultimately, several improvements can be made to the current device to enhance the limited amount of photoelectricity demonstrated in this chapter. Moreover, further research is required to better understand the reasons behind the IX emission locations in the PL map and to evaluate the effects of both intralayer and interlayer excitons on device efficiency. Applying these suggestions may enable the fabrication of a large-area 2D heterostructure PV that can sufficiently and conclusively address the research question.

Chapter 7

Summary and Outlook

7.1 Summary

In this report, we focus on a large-area WS_2/WSe_2 heterostructure device and the role of intralayer and interlayer excitons in its photocurrent generation.

We begin by exfoliating large-area monolayers using gold-assisted exfoliation, followed by the development of a novel polymer-based transfer method that utilises LDPE. This method enables the accurate and consistent transfer of large-area monolayers onto various substrates of varying roughness. Throughout the transfer process, we assess the quality of the monolayer using PL spectroscopy to quantify the exciton quality by measuring the narrowing of the exciton linewidth and observing the uniformity of the wide-field photoluminescence of a WS_2 monolayer.

Next, we employ this transfer method to transfer a WS_2 monolayer followed by a WSe_2 and create a WS_2/WSe_2 heterostructure. We test the physical and electronic overlap through various optical spectroscopy techniques: Raman spectroscopy identifies the physical overlap of the layers, and PL spectroscopy verifies the electronic coupling between the monolayers, which we confirm by observing IX emissions at room temperature. Further confirmation on the existence of the IX is obtained through temperature- and power-dependent PL measurement. The temperature-dependent PL spectra exhibit the expected blue shift and intensity increase with decreasing temperatures. Meanwhile, the power-dependent PL produced α values consistent with the growth rate of near-linear intralayer and sublinear interlayer emissions. Finally, to understand the inherent direct excitation mechanisms employed by the HS, we perform temperature-dependent reflectivity measurements. The resulting lack of peaks at IX wavelengths leads us to suggest that the IX formation involves a two-step process of intralayer exciton creation followed by an interlayer electron transfer.

Following the successful fabrication of a heterostructure, we design a photovoltaic device with gold contacts to maximise the absorption of sunlight. The fabrication of the device involves a three-step process: the transfer of a 35-mm-thick hBN flake, the transfer of the WSe_2 monolayer, and the transfer of the WS_2 layer. Optical characterisation is once again performed to confirm the fabrication of the WSe_2/WS_2 on top of the gold contact and hBN flake, and to confirm the interlayer coupling.

Furthermore, the electrical characterisation of the device revealed its linear I-V response, even under LED illumination. The I-V response also indicated the presence of a high resistance and the lack of a proper junction. Additionally, the EQE measurements provided further insight into the current generation as we observe higher photocurrent at the WS_2 A- and B-exciton wavelengths. Unfortunately, the EQE measurement using a near-infrared or infrared excitation source suffers from high noise, which limits the conclusions we can draw about the excitons in those wavelength ranges.

7.2 Outlook

The gold-assisted exfoliation, followed by large-area LDPE-dependent stamping, has proven to produce large-area, high-quality monolayers and heterostructures reliably. The implementation of this method for further optoelectric experimentation appears promising. However, bottom-up monolayer fabrication techniques, such as CVD, are currently

better suited for commercial photovoltaics, given the ease of scalability and the rapid development of this method [9].

Nonetheless, the development of large-area LDPE-dependent transfer is imperative for creating high-quality 2D heterostructures on various substrates. Further work could involve using this method to fabricate another WSe_2/WS_2 with a clearer electrical junction by stamping the monolayers onto separate contacts. This device could produce a more accurate estimation of the photovoltaic response and power conversion efficiency of the current design.

Apart from that, the device design could be adapted on multiple fronts, such as optimising the metal contact materials. Since contact material is crucial for the contact resistance experienced by the device, metals with more appropriate work functions could produce lower resistances. Additionally, considering asymmetrical metal contacts, such that each is made from a different metal, could lead to increased charge separation. This idea takes into consideration that metal/TMDC interfaces typically exhibit high resistance due to the high Schottky barrier [30]. This leads to an additional avenue of investigation: using interfacial layers sandwiched between the contacts and the 2D material stack to act as an intermediary for charge transfer.

Another critical factor is the geometry of the electrodes. The current design has a 30 μm gap between both contacts, which exceeds the diffusion length of excitons (< tens of μm) [87]. Since the diffusion length is proportional to the square root of the mobility and carrier lifetime [88], future designs should include exciton lifetime measurements to optimise the electrode geometry. Moreover, moving from lateral device configurations towards vertical device configurations could reduce the diffusion length required to reach the electrode. This is a result of vertically stacked contacts, which allow for vertical charge diffusion, thereby limiting the travel distance of electrons to the thickness of the monolayer. Thus, the decrease in travel distance could lead to improvements in the photovoltaic response and overall power conversion efficiency due to higher electron collection.

These investigation pathways are just a few of the ways that 2D heterostructure devices can continue to develop; however, there are still many other aspects to consider and investigate. For example, on the photonic side, examining the integration of large-area devices with photonic enhancers, such as metasurfaces, could prove indispensable for achieving high sunlight absorption. Hence, with 2D materials for photovoltaics being a relatively novel field within the photovoltaics sector, there are still ample opportunities to explore new material combinations and device geometries.

Bibliography

[1] IPCC. *Climate Change 2022: Mitigation of Climate Change. Contribution of Working Group III to the Sixth Assessment Report of the Intergovernmental Panel on Climate Change* (Cambridge University Press, Cambridge, UK and New York, NY, USA, 2022). URL https://www.ipcc.ch/report/ar6/wg3/.

[2] Roser, M. Why did renewables become so cheap so fast? *Our World in Data* (2020). Https://ourworldindata.org/cheap-renewables-growth.

[3] Li, Z., Ma, T., Yang, H., Lu, L. & Wang, R. Transparent and colored solar photovoltaics for building integration. *Solar RRL* **5**, 2000614 (2021). URL https://onlinelibrary.wiley.com/doi/abs/10.1002/solr.202000614. https://onlinelibrary.wiley.com/doi/pdf/10.1002/solr.202000614.

[4] AMOLF. AMOLF NEWS: 75 jaar – Special Edition. https://amolf.nl/wp-content/uploads/2024/10/AMOLF-NEWS-75-jaar-2024-page.pdf (2024). Special issue, pages 22–27, October 2024.

[5] Novoselov, K. S. *et al.* Electric Field Effect in Atomically Thin Carbon Films. *Science* **306** (2004).

[6] Jariwala, D., Davoyan, A. R., Wong, J. & Atwater, H. A. Van der Waals Materials for Atomically-Thin Photovoltaics: Promise and Outlook. *ACS Photonics* **4** (2017).

[7] Sze, S. M. *Physics of Semiconductor Devices* (John Wiley Sons, Inc., 1981).

[8] Bozheyev, F. Advancement of transition metal dichalcogenides for solar cells: a perspective. *Journal of Materials Chemistry A* **11** (2023).

[9] Islam, K. M., Ismael, T., Luthy, C., Kizilkaya, O. & Escarra, M. D. Large-Area, High-Specific-Power Schottky-Junction Photovoltaics from CVD-Grown Monolayer MoS_2. *ACS Applied Materials and Interfaces* **14** (2022).

[10] Paik, E., Zhang, L., Mak, K. F., Shan, J. & Deng, H. Excitons and polaritons in two-dimensional transition metal dichalcogenides: a tutorial. *Advances in Optics and Photonics* **16** (2024).

[11] Tian, S., Zhou, K., Yin, W. & Liu, Y. Machine learning enables the discovery of 2D Invar and anti-Invar monolayers. *Nature Communications* **15** (2024).

[12] Motlagh, S. A. O., Apalkov, V. & Stockman, M. Femtosecond currents in transition metal dichalcogenides monolayers. *Physical Reviews B* **103**, 155416 (2020).

[13] Chhowalla, M. *et al.* The chemistry of two-dimensional layered transition metal dichalcogenide nanosheets. *Nature Chemistry* **5**, 263–275 (2013).

[14] Manzeli, S., Ovchinnikov, D., Pasquier, D., Yazyev, O. V. & Kis, A. 2D transition metal dichalcogenides. *Nature Reviews Materials* **2** (2017).

[15] Fox, M. *Optical Properties of Solids* (Oxford University Press, 2010).

[16] Chernikov, A. *et al.* Exciton Binding Energy and Nonhydrogenic Rydberg Series in Monolayer WS_2. *Physical Review Letters* **113** (2014).

[17] Li, Y. *et al.* Measurement of the optical dielectric function of monolayer transition-metal dichalcogenides: MoS_2, $MoSe_2$, WS_2, and WSe_2. *Physical Reviews B* **90**, 205422 (2014).

[18] Wilson, N. R. *et al.* Determination of band offsets, hybridization, and exciton binding in 2d semiconductor heterostructures. *Science Advances* **3**, e1601832 (2017). URL https://www.science.org/doi/abs/10.1126/sciadv.1601832. https://www.science.org/doi/pdf/10.1126/sciadv.1601832.

[19] Yu, J. *et al.* Observation of double indirect interlayer exciton in WSe_2/WS_2 heterostructure. *Scientific Reports* **28** (2020).

[20] Fang, H. *et al.* Localization and interaction of interlayer excitons in $MoSe_2$/WSe_2 heterobilayers. *Nature Communications* **14** (2023).

[21] Montblanch, A. R.-P. *et al.* Confinement of long-lived interlayer excitons in WS_2/WSe_2 heterostructures. *Communications Physics* **4** (2021).

[22] Durmuş, M. A. & Sarpkaya, I. Quantum Beats between Spin-Singlet and Spin-Triplet Interlayer Exciton Transitions in WSe_2–$MoSe_2$ Heterobilayers. *Nano Letters* **24**, 5767–5773 (2024).

[23] Fu, Y., Long, M., Gao, A. & Wang, Y. Intrinsic p-type W-based transition metal dichalcogenide by substitutional Ta-doping. *Applied Physics Letters* **111** (2017).

[24] Cho, S. B. & Chung, Y.-C. Band engineering in a van der Waals heterostructure using a 2D polar material and a capping layer. *Scientific Reports* **6** (2016).

[25] Nazif, K. N. *et al.* High-specific-power flexible transition metal dichalcogenide solar cells. *Nature Communications* **12** (2021).

[26] Roy, S. & Bermel, P. A new metal transfer process for van der Waals contacts to vertical Schottky-junction transition metal dichalcogenide photovoltaics. *Solar Energy Materials and Solar Cells* **174** (2018).

[27] Fontana, M. *et al.* Electron-hole transport and photovoltaic effect in gated MoS_2 Schottky junctions. *Scientific Reports* **3** (2013).

[28] Choi, M. S. *et al.* Lateral MoS_2 p–n Junction Formed by Chemical Doping for Use in High-Performance Optoelectronics. *ACS Nano* **8** (2014).

[29] Went, C. M. *et al.* A new metal transfer process for van der Waals contacts to vertical Schottky-junction transition metal dichalcogenide photovoltaics. *Science Advances* **5** (2019).

[30] Farmanbar, M. & Brocks, G. Ohmic Contacts to 2D Semiconductors through van der Waals Bonding. *Advanced Electronic Materials* **2**, 1500405 (2016).

[31] Özçelik, V. O., Azadani, J. G., Yang, C., Koester, S. J. & Low, T. Band alignment of two-dimensional semiconductors for designing heterostructures with momentum space matching. *Physical Reviews B* **94**, 035125 (2016).

[32] Lin, P. & Yang, J. Tunable WSe_2/WS_2 van der Waals heterojunction for self-powered photodetector and photovoltaics. *Journal of Alloys and Compounds* **842**, 155890 (2020).

[33] Pan, Y. & Zahn, D. R. T. Raman Fingerprint of Interlayer Coupling in 2D TMDCs. *Nanomaterials* **12**, 3949 (2022).

[34] Tuschel, D. Practical Group Theory and Raman Spectroscopy, Part I: Normal Vibrational Modes. *Spectroscopy* **29**, 14 (2014).

[35] Wu, K. *et al.* Helicity-Resolved Vibrational Coupling in Twist WS_2/WSe_2 Heterostructures. *ACS Applied Materials and Interfaces* **16**, 44186–44192 (2024).

[36] He, Y.-M., Höfling, S. & Schneider, C. Phonon induced line broadening and population of the dark exciton in a deeply trapped localized emitter in monolayer wse2. *Opt. Express* **24**, 8066–8073 (2016). URL `https://opg.optica.org/oe/abstract.cfm?URI=oe-24-8-8066`.

[37] Lindholm, F. A., Fossum, J. G. & Burgess, E. L. Application of the superposition principle to solar-cell analysis. *IEEE Transactions on Electron Devices* **26**, 165–171 (1979).

[38] Ali, N. *et al.* Beyond lead: Progress in stable and non-toxic lower-dimensional perovskites for high-performance photodetection. *Sustainable Materials and Technologies* **38**, e00759 (2023).

[39] Huang, Y. *et al.* Universal mechanical exfoliation of large-area 2D crystals. *Nature Communciations* **11** (2020).

[40] Kang, T. *et al.* Strategies for Controlled growth of Transition Metal Dichalcogenides by Chemical Vapor Deposition for Integrated Electronics. *ACS Materials Au* **2** (2022).

[41] Wang, Z., Lin, K. & Zhao, Y.-P. The effect of sharp solid edges on the droplet wettability. *Journal of Colloid and Interface Science* **552**, 563–571 (2019).

[42] Laminated Plastics, Inc. Low density polyethylene (ldpe) technical data sheet. `https://laminatedplastics.com/ldpe.pdf` (n.d.). Accessed: 2025-07-01.

[43] Parbhoo, B., O'Hare, L.-A. & Leadley, S. *The Mechanics of Adhesion* (Elsevier Science, 2002).

[44] Vorvolakos, K. & CHaudhury, M. K. The Effects of Molecular Weight and Temperature on the Kinetic Friction of Silicone Rubbers. *Langmuir* **19**, 6778–6787 (2003).

[45] Wilkes, C. E. & Berard, M. T. *PVC Handbook* (Hanser, 2005).

[46] Kudzin, M. H., Piwowarska, D., Festinger, N. & Chruściel, H. J. Risks Associated with the Presence of Polyvinyl Chloride in the Environment and Methods for Its Disposal and Utilization. *Materials (Basel)* **17** (2023).

[47] California Pacific Lab. Chemical compatibility and resistance charts. `https://www.calpaclab.com/chemical-charts` (2025). Accessed: 2025-07-01.

[48] Solomons, T. W. G. & Fryhle, C. B. *Organic Chemistry* (John Wiley & Sons, Hoboken, NJ, 2009), 10 edn.

[49] Wong, S. L., Ngadi, N. & Abdullah, T. A. T. Study on Dissolution of Low Density Polyethylene (LDPE). *Applied Mechanics and Materials* **695**, 170–173 (2014).

[50] European Chemicals Agency (ECHA). Xylene — registration dossier — physical and chemical properties. `https://echa.europa.eu/registration-dossier/-/registered-dossier/15448/4/12` (2025). Accessed: 2025-07-10.

[51] National Institute for Occupational Safety and Health (NIOSH). Niosh pocket guide to chemical hazards — trichloroethylene. `https://www.cdc.gov/niosh/npg/npgd0629.html` (2025). Accessed: 2025-07-10.

[52] Amani, M. *et al.* Near-unity photoluminescence quantum yield in mos₂. *Science* **350**, 1065–1068 (2015). URL `https://www.science.org/doi/abs/10.1126/science.aad2114`. `https://www.science.org/doi/pdf/10.1126/science.aad2114`.

[53] Tanoh, A. O. A. *et al.* Enhancing Photoluminescence and Mobilities in WS_2 Monolayers with Oleic Acid Ligands. *Nano Letters* **19**, 6299–6307 (2019).

[54] Young, J. A. Chemical laboratory information profile: Oleic acid. *Journal of Chemical Education* **79**, 24 (2002). URL `https://doi.org/10.1021/ed079p24`. `https://doi.org/10.1021/ed079p24`.

[55] National Institute for Occupational Safety and Health (NIOSH). Oleic acid - international chemical safety cards (icsc). `https://iiab.me/modules/en-cdc/www.cdc.gov///niosh/ipcsneng/neng1005.html` (2025). Accessed: 2025-07-09.

[56] Tanoh, A. O. A. *et al.* Giant photoluminescence enhancement in $MoSe_2$ monolayers treated with oleic acid ligands. *Nanoscale advances* **3**, 4216–4225 (2021).

[57] Daniel, L. *et al.* Mechanism of oleic acid-mediated sulfur vacancy healing in monolayer ws_2 (2025). URL `https://arxiv.org/abs/2501.17536`. `2501.17536`.

[58] Nosal, H. *et al.* Selected Fatty Acids Esters as Potential PHB-V Bioplasticizers: Effect on Mechanical Properties of the Polymer. *Journal of Polymers and the Environment* **29**, 38–53 (2021).

[59] Shin, K. H., Seo, M.-K., Pak, S., Jang, A.-R. & Sohn, J. I. Observation of strong interlayer couplings in ws2/mos2 heterostructures via low-frequency raman spectroscopy. *Nanomaterials* **12** (2022). URL `https://www.mdpi.com/2079-4991/12/9/1393`.

[60] Wang, K. *et al.* Interlayer coupling in twisted wse2/ws2 bilayer heterostructures revealed by optical spectroscopy. *ACS Nano* **10**, 6612–6622 (2016). URL https://doi.org/10.1021/acsnano.6b01486. PMID: 27309275, https://doi.org/10.1021/acsnano.6b01486.

[61] Fu, Q. *et al.* Room-temperature efficient and tunable interlayer exciton emissions in WS_2/WSe_2 heterobilayers at high generation rates. *Optics Letters* **49** (2024).

[62] Hanbicki, A., Currie, M., Kioseoglou, G., Friedman, A. & Jonker, B. Measurement of high exciton binding energy in the monolayer transition-metal dichalcogenides ws2 and wse2. *Solid State Communications* **203**, 16–20 (2015). URL http://dx.doi.org/10.1016/j.ssc.2014.11.005.

[63] Schmidt, U. *et al.* A comprehensive study of wse_2 crystals using correlated raman, photoluminescence (pl), second harmonic generation (shg), and atomic force microscopy (afm) imaging. *Spectroscopy Online* **36**, 23–30 (2021). URL https://www.spectroscopyonline.com/view/a-comprehensive-study-of-wse2-crystals-using-correlated-raman-photoluminescence-pl-second-harmonic-generation-shg-and-atomic-force-microscopy-afm-imaging.

[64] Tyurnina, A. *et al.* Strained bubbles in van der Waals heterostructures as local emitters of photoluminescence with adjustable wavelength. *ACS Photonics* **6**, 516–524 (2019).

[65] Nayak, P. K. *et al.* Probing evolution of twist-angle-dependent interlayer excitons in $mose_2$/wse_2 van der waals heterostructures. *ACS Nano* **11**, 4041–4050 (2017).

[66] Yuan, L. *et al.* Twist-angle-dependent interlayer exciton diffusion in ws_2–wse_2 heterobilayers. *Nature Materials* **19**, 617–623 (2020).

[67] Alexeev, E. M. *et al.* Emergence of highly linearly polarized interlayer exciton emission in mose2/wse2 heterobilayers with transfer-induced layer corrugation. *ACS Nano* **14**, 11110–11119 (2020). URL http://dx.doi.org/10.1021/acsnano.0c01146.

[68] Carozo, V. *et al.* Optical identification of sulfur vacancies: Bound excitons at the edges of monolayer tungsten disulfide. *Science Advances* **3** (2017).

[69] Kai, F. *et al.* Distinct moiré exciton dynamics in WS_2/WSe2 heterostructure. *Quantum Frontiers* **4** (2025).

[70] Gerber, I. C. & Marie, X. Dependence of the hBN Layer Thickness on the Band Structure and Exciton Properties of Encapsulated WSe_2 Monolayers. *Physical Reviews B* **98**, 245126 (2018).

[71] Hu, Y. *et al.* All-Optical Valley Polarization Switch via Controlling Spin-Triplet and Spin-Singlet Interlayer Exciton Emission in WS_2/WSe_2 Heterostructure. *Nano Letters* **23**, 6581–6587 (2023).

[72] Huang, J., Hoang, T. B. & Mikkelsen, M. H. Probing the origin of excitonic states in monolayer WSe_2. *Scientific Reports* **6** (2016).

[73] Gupta, N., Sachin, S., Kumari, P., Rani, S. & Ray, S. J. Twistronics in two-dimensional transition metal dichalcogenide (tmd)-based van der waals interface. *RSC Adv.* **14**, 2878–2888 (2024). URL http://dx.doi.org/10.1039/D3RA06559F.

[74] Byrnes, S. J. Multilayer optical calculations (2020). 1603.02720.

[75] Dykstra, P. H. Time-dependent photoluminescence in silicon. Tech. Rep. NASA TM-80024, NASA Lewis Research Center (1979). URL https://ntrs.nasa.gov/citations/19800007296.

[76] Illiarionov, Y. Y. *et al.* Insulators for 2D nanoelectronics: the gap to bridge. *Nature Communications* **11**, 3385 (2020).

[77] ASTM International. ASTM G173-03(2020): Standard Tables for Reference Solar Spectral Irradiances: Direct Normal and Hemispherical on 37° Tilted Surface. ASTM International Standard (2020). Available from: https://www.astm.org/g0173-03r20.html.

[78] Mozetič, M. Aging of plasma-activated polyethylene and hydrophobic recovery of polyethylene polymers. *Polymers* **15** (2023). URL `https://www.mdpi.com/2073-4360/15/24/4668`.

[79] Novotny, L. & Hecht, B. *Principles of Nano-Optics* (Cambridge University Press, 2006).

[80] Waheed, Y. *et al.* Large trion binding energy in monolayer WS_2 via strain-enhanced electron–phonon coupling. *Communications Materials* **6** (2025).

[81] Moody, G. *et al.* Intrinsic homogeneous linewidth and broadening mechanisms of excitons in monolayer transition metal dichalcogenides. *Nature Communications* **6** (2015).

[82] Di Bartolomeo, A. *et al.* Hysteresis in the transfer characteristics of MoS_2 transistors. *2D Materials* **5**, 015014 (2017).

[83] Ghani, F., Duke, M. D. & Carson, J. K. Numerical calculation of series and shunt resistances and diode quality factor of a photovoltaic cell using the Lambert W-function. *Solar Energy* **91**, 422–431 (2013).

[84] Shen, P.-C. *et al.* Ultralow contact resistance between semimetal and monolayer semiconductors. *Nature* **593**, 211–217 (2021).

[85] Maissel, L. I. & Glang, R. (eds.) *Handbook of Thin Film Technology* (McGraw-Hill, New York, 1970), 1st edn.

[86] Luong, D. H. *et al.* Tunneling photocurrent assisted by interlayer excitons in staggered van der waals heterobilayers. *Advanced Materials* **29**, 1701512 (2017).

[87] Rossi, A. *et al.* Anomalous Interlayer Exciton Diffusion in WS_2/WSe_2 Moiré Heterostructure. *ACS Nano* **18**, 18202–18210 (2024).

[88] Frohna, K. & Stranks, S. D. *Handbook of Organic Materials for Electronic and Photonic Devices*. Woodhead Publishing Series in Electronic and Optical Materials (Woodhead Publishing, 2019).

Acknowledgements

I would like to thank all the following people, without whose constant support over the past year this thesis would not have been possible.

First of all, I would like to thank Jorik van de Groep for giving me the opportunity to work on such an intriguing project and for supervising throughout. His guidance allowed me to steadily and carefully develop my project, even during these unusually busy days. Many thanks to Tom Hoekstra for helping me with measurements, answering countless questions, and providing invaluable feedback to refine my thesis. I also want to thank Bernardo Dias for training me on various techniques vital to this thesis (including exfoliation), collaborating on the development of the large-area stamping method, and patiently answering my many questions.

Thanks to Mehmet Atif Durmuş for helping me interpret the cryostat data and understand the effect of interlayer excitons, as well as for the constant stream of jokes and memes that broke the day's monotony. I also thank Reynolds Dziobek-Garrett for sharing his experience and expertise in both TMDCs and experimental setups, particularly the TCSPC and the cryostat. Thanks to Eva Almeida for her helpful discussions and explanations about IV measurements, her expertise in photovoltaics, and the great conversations in between. Many thanks to Cian Dooley for being my quasi-lab partner, always lending an ear, and helping find solutions through our many conversations. Thanks to Freek van Gorp for always offering excellent suggestions, whether they are computer-related, analysis-related, or writing-related. Thanks also to Alex Lambertz and Thomas Bauer for their assistance with the EQE and the cryostat. Thanks to David van Houten for measuring the intralayer and interlayer exciton lifetimes of my sample. Although I was unable to discuss the results due to time constraints, they hold a place of honour in my appendix. In general, I want to thank everyone in the 2D Nanophotonics group and in Quantum Materials for creating such a pleasant environment.

Last but not least, my heartfelt thanks to my family for all their support. Thank you, Paolo and Julian, for listening to me ramble about my weekly progress. And most importantly, thank you, Mom and Dad, for your unwavering belief in me and your constant encouragement, which helped me push forward when I was stuck and frustrated.

Chapter A

Time-Resolved Photoluminescence

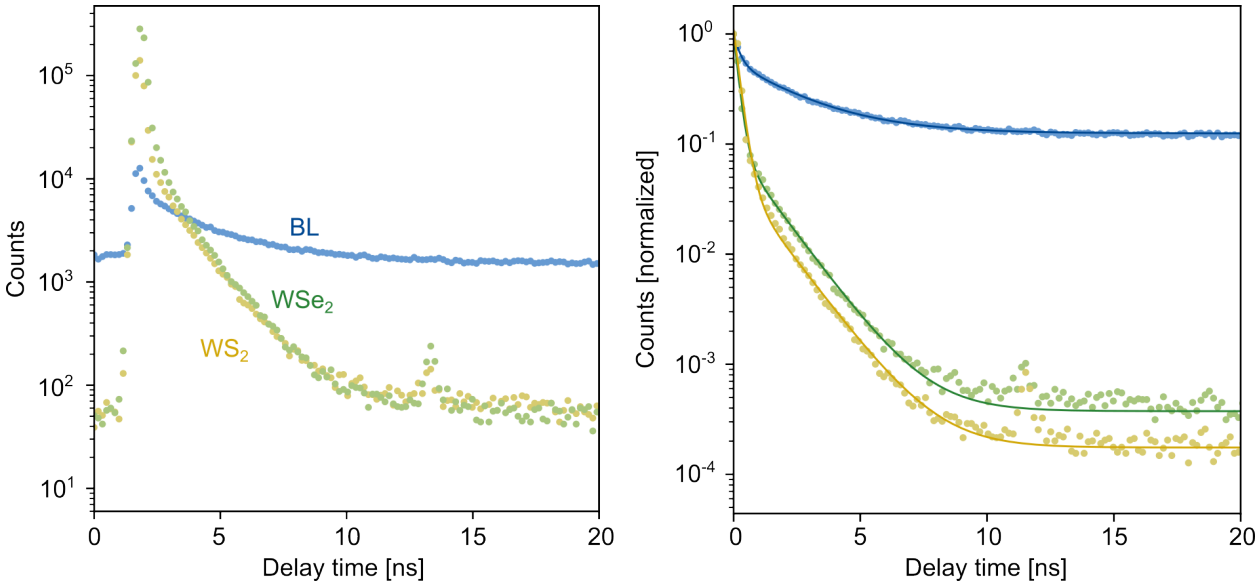

Figure A.1: Time-resolved photoluminescence spectra of a WSe_2/WS_2 HS at 3 K, excited with a low-power 445 nm pulsed laser at 20 MHz. The spectra correspond to the WS_2 intralayer exciton (yellow), the WSe_2 intralayer exciton (green), and the IX (BL, Blue). The raw data (left) are acquired with exposure times of < 1 minute for the intralayer excitons and ~70 minutes for the IX. Additionally, all measurements utilised different optical filters to isolate each signal: 600nm/40nm FWHM bandpass for WS_2, 750nm/40nm FWHM bandpass for WSe_2, and 830 nm longpass for the IX. The normalised data (right) facilitates direct comparison of different exciton lifetimes. Visual inspection reveals longer decay tails for the IX, which is consistent with literature. Qualitatively, the bi-exponential decay fitting yields the respective fast and slow lifetime components of each exciton: 0.184 ns / 1.385 ns (WS_2 intralayer exciton), 0.226 ns / 1.417 ns (WSe_2 intralayer exciton), and 0.248 ns / 2.561 ns (IX), such that the IX decay is at least 1 ns slower than the intralayer excitons.